Temperature and intrinsic Ca^{2+} reshape TRPM4 pharmacology

Jinhong Hu[1], Sofia Ievleva[1], Sung Jin Park[1], Junuk Lee[1], Jennifer Cheng[1], Garrett O'Dea[1], Jiangnan Sheng[1], Juan Du[#1,2,3] & Wei Lü[#1,2,3]

1. Department of Molecular Biosciences, Northwestern University, Evanston, IL, USA
2. Department of Pharmacology, Feinberg School of Medicine, Northwestern University, Chicago, IL, USA
3. Chemistry of Life Processes Institute, Northwestern University, Evanston, IL, USA

#CORRESPONDING AUTHOR

Correspondence and requests for materials should be addressed to J. D. (email: juan.du@northwestern.edu) TEL: (847) 467-6719, or W. L. (email: wei.lu@northwestern.edu). TEL: (847) 491-5440

Abstract

Proteins operate in dynamic environments where ions, lipids, and temperature collectively define their properties, yet most studies rely on simplified conditions that overlook these intrinsic variables. Here, we show two such factors—temperature and Ca^{2+}—profoundly remodel the function and pharmacology of TRPM4, an ion channel implicated in cardiac conduction, immune regulation, and cancer. At physiological temperature and Ca^{2+}, TPPO—previously considered a selective TRPM5 inhibitor inactive toward TRPM4—potently activates TRPM4, revealing strong synergy among temperature, Ca^{2+}, and ligand binding. In contrast, Necrocide-1, a necroptotic activator targeting the same binding pocket, defies this logic: it opens TRPM4 without Ca^{2+} but is antagonized by Ca^{2+}. Meanwhile, the inhibitors NBA and CBA engage a nearby pocket, locking the channel in a non-conductive pre-open state. Our findings highlight that even rigid binding pockets can exhibit temperature-dependent ligand recognition, revealing hidden pharmacology and informing selective, environment-aware therapeutic strategies.

Introduction

Protein activity is inherently governed by the cellular environment in which it operates. A wide array of factors—including ions, lipids, temperature, pH, and protein–protein interactions—collectively determine how a protein functions in its native context. Yet, because of technical constraints, most biophysical and pharmacological studies have been conducted under simplified conditions, which have yielded foundational insights but often fail to capture the full physiological complexity.

Increasing efforts now aim to bridge this gap by incorporating more native variables—for example, using nanodiscs, liposomes or membrane-derived vesicles to preserve native lipidic environments for membrane proteins[1-4], and purifying proteins from native sources to retain endogenous protein compositions and modifications[5-8]. Despite these advances, one fundamental determinant, temperature, is largely overlooked in mechanistic and pharmacological studies, even though it influences every protein in the human body, where proteins operate at 37°C. Because most in vitro assays are performed at room temperature or lower, therefore, the broad impact of temperature on protein conformation, ligand recognition, efficacy and mechanism remains unexplored, with only a few recent exceptions[9,10].

Alongside temperature, intracellular Ca^{2+} represents another intrinsic physiological variable that exerts pervasive influence on protein behavior. Although not universal, Ca^{2+} acts as a selective yet broad regulator of cellular physiology. It is among the most tightly controlled cellular cofactors, with cytosolic concentrations fluctuating dynamically from tens of nanomolar at rest to low micromolar during signaling, and rising to abnormally high levels under pathological conditions such as ischemia, excitotoxicity, or cancer[11]. Many proteins are directly regulated by Ca^{2+} through dedicated binding sites, while others respond indirectly through Ca^{2+}-dependent signaling cascades. Although the structural and functional roles of Ca^{2+} have been extensively characterized, its impact on protein–ligand interactions—particularly in combination with other intrinsic factors like temperature—has rarely been considered. This represents an important gap in our understanding of how Ca^{2+}-regulated proteins engage ligands under physiological and pathological conditions.

The Ca^{2+}-activated, temperature-sensitive channel Transient Receptor Potential Melastatin 4 (TRPM4) provides an ideal model to investigate how intrinsic physiological factors remodel

pharmacology[12-15]. TRPM4 is a non-selective monovalent cation channel that contributes to cardiac conduction, insulin secretion, neuronal excitability, immune regulation, and intestinal fluid homeostasis[16-25]. Pathogenic variants have been implicated in Brugada syndrome, inherited conduction disorders, and diverse cancers[26-34]. Despite its broad physiological and pathological relevance, TRPM4 has remained largely untargeted by clinical pharmacology, with the single exception of bisacodyl—a widely used drug for chronic constipation—and its active metabolite deacetyl bisacodyl, which we recently identified and characterized as clinically relevant TRPM4 ligands[25].

Previous structural and functional studies established that TRPM4 adopts two major conformations, a "cold" and a "warm" state, whose equilibrium depends on both temperature and cytosolic Ca^{2+} concentration[10]. These findings suggest that biophysical and pharmacological assays performed under room temperature and undefined Ca^{2+} conditions may not accurately capture the channel's behavior under physiological settings.

Here, we systematically examine TRPM4 pharmacology under conditions that incorporate both temperature and Ca^{2+}. Through combined cryo-EM and electrophysiology, we reveal that these intrinsic factors profoundly shape ligand recognition, efficacy, and mechanism. Our results identify the S1–S4 domain as a dynamic regulatory hub that integrates environmental and chemical cues to govern activation and inhibition. More broadly, this work establishes an environment-aware framework for pharmacology, in which incorporating intrinsic variables exposes hidden drug activities and new mechanisms of regulation. For widely expressed proteins like TRPM4, such principles open opportunities to design therapeutics that exploit pathological local conditions—such as abnormally elevated Ca^{2+} or altered thermal states—for selective action in disease, while preserving normal physiological function and minimizing side effects.

Results

Temperature reveals hidden pharmacology of TRPM4

During the cold-to-warm transition of TRPM4, Ca^{2+} and temperature drive major conformational changes in the intracellular domain but only subtle shifts in the transmembrane domain[10]. From these structures, we identified three categories of ligand binding sites that emerge elusively in the warm conformation of the intracellular domain[10]. While this outcome may be anticipated from

the magnitude of ICD rearrangement, it nevertheless raises two central questions: whether drug screening performed exclusively at room temperature may have overlooked active compounds, and whether temperature-dependent ligand recognition is confined to regions undergoing large conformational change (such as the intracellular domain) or extends to regions with more modest movements (such as the transmembrane domain).

To address these questions, we examined several previously reported TRPM4 ligands, as well as compounds considered inactive toward TRPM4. We focused on hydrophobic ligands predicted to interact with the transmembrane domain, including triphenylphosphine oxide (TPPO), necrocide-1 (NC1), and the anthranilic acid derivatives CBA (4-chloro-2-[2-(2-chloro-phenoxy)-acetylamino]-benzoic acid) and NBA (4-chloro-2-(2-(naphthalene-1-yloxy) acetamido) benzoic acid). TPPO, originally identified as a selective TRPM5 inhibitor with an IC_{50} of 12 μM, has been found inactive on TRPM4 when tested at room temperature using fluorescence-based membrane potential assays[35]. NC1 was recently characterized as a TRPM4 activator that promotes Na^+ influx and triggers necrotic cell death[36], suggesting therapeutic potential in cancer. NBA and CBA represent the best-characterized TRPM4 inhibitors to date with IC_{50} in the sub-micromolar range[37]. Importantly, all prior functional and structural studies were conducted at room temperature or lower.

Using patch-clamp electrophysiology, we tested these compounds at both room temperature and 37°C. Under previously reported assay conditions—room temperature with either zero free intracellular Ca^{2+} or basal free intracellular Ca^{2+} (100 nM), we reproduced established results: 50 μM TPPO showed negligible activity on TRPM4—comparable to the control group, where basal Ca^{2+} alone is insufficient to drive channel activation (Fig. 1a,b; Extended Data Fig. 1a,b); NC1 activated the channel, eliciting largely linear, voltage-independent currents (Fig. 2a,b); and NBA and CBA produced robust inhibition of Ca^{2+}-induced TRPM4 current (Extended Data Fig. 2a). Strikingly, elevating the temperature to 37°C revealed a hidden pharmacological behavior. While NC1, NBA, and CBA retained their room-temperature profiles (Fig. 2d,e; Extended Data Fig. 2a), TPPO displayed a completely different response—robustly activating TRPM4 currents (Fig. 1e; Extended Data Fig. 1e). These observations highlight a critical gap in conventional pharmacological screening: assays performed under non-physiological conditions may both overlook potential active compounds and misclassify ligand selectivity.

128 **Ca^{2+} as a key determinant of agonist recognition and potency in TRPM4**

129 Ca^{2+} is the only known endogenous agonist of TRPM4, and together with temperature, drives the
130 transition between its cold to warm conformations[10]. Building on our findings that temperature
131 reshapes TRPM4 pharmacology (Fig. 1e), we next explored whether Ca^{2+} modulates the binding
132 and potency of the exogenous activators TPPO and NC1.

133 Under Ca^{2+}-free conditions achieved by EGTA buffering, 50 uM TPPO produced negligible
134 activation of TRPM4 (Fig. 1d; Extended Data Fig. 1d), whereas adding 100 nM free intracellular
135 Ca^{2+} enabled robust activation (Fig. 1e, red traces; Extended Data Fig. 1e). Thus, even basal Ca^{2+}
136 concentrations—although insufficient to open the channel alone (Fig. 1e, black trace; Extended
137 Data Fig. 1e)—markedly enhance TPPO-induced TRPM4 activation. To quantify this apparent
138 synergy, we determined TPPO dose-response relationships. Physiological temperature increased
139 TPPO potency by ~14-fold under basal Ca^{2+} (Fig. 1g,h; Extended Data Fig. 1g,h), while basal
140 Ca^{2+} increased TPPO potency by ~6-fold at 37 °C (Fig. 1g,i; Extended Data Fig. 1g,i). In the
141 absence of both Ca^{2+} and physiological temperature, TPPO activated TRPM4 only weakly at
142 submillimolar concentrations and failed to reach saturation even at millimolar levels. When
143 intracellular Ca^{2+} reach activating level (1 μM), the effect of TPPO is largely masked, consistent
144 with the notion that TPPO and Ca^{2+} act though a shared activation pathway, with Ca^{2+}
145 dominating at high concentration, as both produce the hallmark outwardly rectified currents (Fig.
146 1c,f; Extended Data Fig 1c,f).

147 Together, these data demonstrate that physiological context is essential for TPPO efficacy,
148 revealing a three-way synergy between temperature, Ca^{2+}, and ligand binding. This context
149 dependence overturns the view that TPPO is inactive toward TRPM4, revealing instead that it
150 potently activates the channel—opposite to its inhibitory action on the closely related TRPM5[35].
151 This finding underscores how ligand behavior can be fundamentally mischaracterized when
152 assays are performed under non-physiological conditions.

153 We next examined whether Ca^{2+} influences NC1, previously reported as the first Ca^{2+}-
154 independent agonist of TRPM4[36]. Under Ca^{2+}-free and 100 nM Ca^{2+} conditions, NC1 evoked
155 nearly identical currents with linear current-voltage relationships distinct from Ca^{2+}-activated
156 currents, confirming that NC1 can activate TRPM4 independently with an EC_{50} in the
157 submicromolar range (Fig. 2a,b,d,e,g,h; Extended Data Fig. 3a). However, at 1 μM Ca^{2+}, a

158 physiologically relevant level during cellular stress that robustly activates TRPM4, the response
159 changed dramatically, becoming strongly outwardly rectified (Fig. 2c,f)—a hallmark of
160 canonical Ca^{2+}-mediated activation[14]. This striking reversal suggests that NC1 is not simply
161 Ca^{2+}-independent: once Ca^{2+} reaches activating levels, its action dominates, functionally
162 overriding NC1-mediated gating even at saturating NC1 concentrations (Fig. 2i). Thus, rather
163 than bypassing the Ca^{2+} requirement, NC1 displays a biphasic Ca^{2+} dependence: permissive at
164 basal Ca^{2+} yet antagonized at higher concentrations, likely either through binding competition or
165 allosteric coupling between NC1 and Ca^{2+} binding sites. This mechanism is discussed further in
166 the section "Mechanistic basis for Ca^{2+}-dependent gating reversal of NC1".

167 Taken together, these results reveal distinct modes of Ca^{2+}-agonist interplay in TRPM4.
168 TPPO requires basal Ca^{2+} (and temperature) to act effectively on the channel, whereas NC1
169 functions independent of Ca^{2+} at rest but loses efficacy once Ca^{2+} rises to stimulatory levels. This
170 contrast illustrates how the same intrinsic cofactor can differentially tune ligand action through
171 cooperative or antagonistic coupling. More broadly, they reinforce the importance of evaluating
172 ion channel pharmacology under physiological conditions, as environmental context can
173 fundamentally alter both efficacy and apparent selectivity.

174 **Structural basis of the three-way synergy between TPPO, temperature and Ca^{2+}**

175 To elucidate how temperature and Ca^{2+} shape TPPO activation of TRPM4, we determined cryo-
176 EM structures of the channel in the presence of TPPO at 18 °C and 37 °C, under both Ca^{2+}-free
177 and Ca^{2+}-saturated conditions. All the structures were resolved to high quality at ~2.5–2.9 Å
178 resolutions, allowing unambiguous identification of ligand binding sites (Extended Data Figs. 4–
179 6; Extended Data Table 1).

180 In the consensus map of the Ca^{2+}/TPPO–TRPM4–37°C dataset, we observed a prominent
181 tripod-shaped density in the S1–S4 domain of each protomer. This feature closely matches the
182 shape of TPPO, and sits immediately above the Ca_{TMD} site (Fig. 3a). We therefore designated this
183 pocket as the S1–$S4_{Upper}$ site. This site spatially overlaps with the deacetyl bisacodyl binding
184 pocket we identified previously[25]. Subunit-level classification revealed that where warm and cold
185 conformations coexist in this dataset, with the warm state predominating (Extended Data Fig. 4).
186 The ligand density is markedly stronger in the warm state, whereas a weaker yet still discernible
187 density exists in the cold state (Fig. 3d; this minor cold state is discussed at the end of this

188 section). Within this pocket, TPPO occupies a hydrophobic cavity and forms a critical polar
189 interaction between its phosphoryl moiety and R1072 on the TRP helix (Fig. 3d, left panel). To
190 validate this assignment, we mutated key coordinating residues to alanine and performed
191 electrophysiological recording. Most mutations impaired Ca^{2+}-dependent activation, likely by
192 disrupting the integrity of the adjacent Ca_{TMD} site, making it impossible to unambiguously isolate
193 their effects on TPPO, as TPPO requires Ca_{TMD} to manifest its activity (Extended Data Fig. 1j).
194 In contrast, R1072A preserved Ca^{2+}-evoked gating yet abolished TPPO-dependent activation,
195 thereby confirming the functional relevance of the TPPO binding site (Extended Data Fig. 1k).

196 In the Ca^{2+}-bound cold conformation from the Ca^{2+}/TPPO–TRPM4–18°C dataset, only a
197 faint and incomplete signal was discernible at the S1–$S4_{Upper}$ site at very low contour levels (Fig.
198 3b). The density formed a triangular outline reminiscent of TPPO but was markedly smaller than
199 the full ligand, consistent with partial or unstable occupancy. In the Ca^{2+}-free cold conformation
200 from the EGTA/TPPO–TRPM4–37°C dataset, this feature disappeared entirely, with no trace of
201 TPPO density detectable (Fig. 3c).

202 Thus, TPPO binding exhibits a clear dependence on the cold–warm conformational
203 equilibrium of TRPM4, a transition that is cooperatively governed by temperature and Ca^{2+}
204 (ref[10]). This structural observation coincides with our electrophysiological finding that TPPO,
205 temperature, and Ca^{2+} act in three-way synergy to promote channel activation (Fig. 1a,b,d,e).
206 Together, these results suggest that TPPO efficacy is tightly coupled to the conformational
207 landscape defined by these two intrinsic modulators.

208 To dissect the mechanism underlying this coupling, we compared the Ca^{2+}-free cold and
209 Ca^{2+}/TPPO-bound warm structures. In the Ca^{2+}-free cold conformation, R1072 is displaced from
210 the S1–$S4_{Upper}$ pocket and stabilized by an interaction with Q831 on S2—a key residue involved
211 in Ca_{TMD} binding—thereby precluding TPPO binding (Fig. 3e). Upon transition to the warm
212 state, upward movement of the intracellular domain tilts the TRP helix, moving R1072 into
213 position for TPPO coordination (Fig. 3e). Concurrently, Ca^{2+} binding at the Ca_{TMD} site recruits
214 Q831 for Ca^{2+} coordination, releasing R1072 from its locked pose for direct interaction with the
215 TPPO phosphoryl group (Fig. 3e). Together, these coupled rearrangements prime the S1–$S4_{Upper}$
216 pocket for effective ligand engagement.

217 Interestingly, a weak TPPO-shaped density was also detected in the minor Ca^{2+}-bound cold
218 conformation present in the Ca^{2+}/TPPO–TRPM4–37°C dataset, identified through single-subunit
219 classification (Extended Data Fig. 4). This density was weaker than in the warm conformation
220 but stronger than in the corresponding Ca^{2+}-bound cold conformation resolved at 18°C (Fig. 3b,
221 lower panel; Fig. 3d; Extended Data Fig. 7), indicating that TPPO occupancy increases with
222 temperature even within the same overall protein conformation. Because the backbone
223 architecture of the binding site remains nearly identical between the two cold structures, this
224 enhancement likely arises from subtle, temperature-dependent sidechain rearrangements—below
225 the resolution of our maps (~2.6 Å local)—that fine-tune ligand packing and render the
226 interaction thermodynamically more favorable.

227 Together, these results reveal that TPPO selectively engages the warm conformation of
228 TRPM4 by exploiting temperature- and Ca^{2+}-dependent changes in local binding energetics. This
229 provides a direct structural basis for the observed three-way synergy, illustrating how intrinsic
230 modulators reshape the binding pocket to control ligand efficacy at the atomic level.

231 **Mechanistic basis for Ca^{2+}-dependent gating reversal of NC1**

232 Building on our observation that NC1 activates TRPM4 in the absence of Ca^{2+} but loses efficacy
233 once Ca^{2+} reaches activating levels (Fig. 2a–f), we sought to define the structural basis of this
234 gating reversal. To this end, we determined cryo-EM structures of TRPM4 in complex with NC1
235 at 37 °C under Ca^{2+}-free and Ca^{2+}-bound conditions, resolved to 2.6 and 2.8 Å, respectively
236 (Extended Data Figs. 6,8; Extended Data Table 2).

237 In the Ca^{2+}-free dataset, a well-defined tripod-shaped density was observed in the S1–S4
238 domain (~2.6 Å local resolution), occupying the same pocket as the TPPO and deacetyl
239 bisacodyl binding sites[25], while no Ca^{2+} density appeared at the Ca_{TMD} site, as expected (Fig. 4a).
240 The shape and dimensions of this density unambiguously matched NC1, which, despite being
241 larger than TPPO, adopts a comparable three-ring scaffold with its indolinone carbonyl oxygen
242 positioned analogously to TPPO's phosphoryl oxygen (Figs. 3d, left panel; Fig. 4a).
243 Consequently, NC1 binds in a similar pose to TPPO, engaging an equivalent network of residues,
244 including a key polar contact between its indolinone carbonyl oxygen and R1072 on the TRP
245 helix (Fig. 4a). Consistent with this, alanine substitution of R1072 and other residues within the

binding site abolished or markedly reduced NC1-mediated activation (Fig. 4c; Extended Data Fig. 3b), confirming that NC1, like TPPO, binds to the S1–S4$_{Upper}$ site.

Interestingly, in the Ca^{2+}-bound dataset, NC1 density at the same S1–S4$_{Upper}$ pocket was markedly weaker (Fig. 4b). This diminished occupancy aligns with our electrophysiological findings, where 1 uM Ca^{2+} strongly suppressed the linear, NC1-evoked currents characteristic of Ca^{2+}-free conditions and restored the canonical Ca^{2+}-dependent gating pattern (Fig. 2a–f). The weak residual density, likely arising from the oversaturating NC1 concentration used for cryo-EM rather than genuine co-binding, supports that NC1 and Ca^{2+} binding are mutually incompatible. Importantly, the antagonism does not result from direct competition for a shared site but instead from allosteric interference between the NC1 pocket and the Ca_{TMD} site (Fig. 4b).

To understand the basis of this interference, we compared the Ca^{2+}-free NC1–TRPM4 and Ca^{2+}–TRPM4 complexes. Two local structural changes accompany Ca^{2+} coordination at the Ca_{TMD}. First, Ca^{2+} binding repositions the TRP helix, shifting R1072 away from the indolinone carbonyl oxygen that is central to NC1 recognition (Fig. 4d). Second, Ca^{2+} binding brings the positively charged R905 into close proximity with NC1's hydrophobic seven-membered cycloheptyl ring, creating an electrostatically unfavorable juxtaposition that further destabilizes ligand binding (Fig. 4d). Together, these antagonistic rearrangements explain why NC1 affinity drops at increased Ca^{2+} concentration.

In summary, NC1 represents the first example of a TRPM4 activator that is temperature-independent yet negatively regulated by intrinsic Ca^{2+}. Structural and functional analyses together uncover a Ca^{2+}-dependent gating reversal, whereby Ca^{2+} reshapes the allosteric network to displace a previously bound activator. This mechanism contrasts sharply with TPPO, whose efficacy requires Ca^{2+} synergy at physiological temperature, underscoring the opposing logic by which intrinsic modulators shape TRPM4 pharmacology.

NC1 overrides Ca^{2+}-dependent ICD–TMD allosteric regulation

The defining feature of NC1 is that it activates TRPM4 without requiring Ca^{2+} at either of the two regulatory sites (Fig. 2a,d): the agonist site Ca_{TMD} and the temperature-dependent allosteric site in the intracellular domain (Ca_{ICD}). In canonical gating, Ca^{2+} and temperature cooperatively couple the ICD and TMD to drive activation: Ca^{2+} binding at the temperature-sensitive Ca_{ICD}

shifts the channel from the cold to the warm state, establishing the primed conformation in which Ca^{2+} binding at the Ca_{TMD} opens the pore at physiologically relevant membrane potentials[10]. To understand how NC1 circumvents this mechanism, we compared three structural states: Ca^{2+}-free cold, Ca^{2+}-bound warm, and NC1-bound. The transition from Ca^{2+}-free cold to Ca^{2+}-bound warm involves major ICD rearrangements coupled to a substantial shift in the TRP helix and TMD (Fig. 4e). By contrast, in the NC1-bound structure the ICD remains in the cold-like, yet the TMD closely resembles the warm state conformation even in the absence of Ca^{2+} at the Ca_{TMD} (Fig. 4f). These observations suggest that NC1 functionally substitutes for Ca^{2+} at the TMD while operating independently of Ca^{2+}-dependent priming at the ICD.

Electrophysiology supported this model: NC1 elicited robust currents of comparable amplitude at both room and physiological temperatures (Fig. 2b,e)—in contrast to Ca^{2+}-dependent TRPM4 activation, which is strongly enhanced at 37 °C through Ca_{ICD}-mediated ICD–TMD coupling[10,15]. Thus, NC1 activates the channel without engaging the Ca_{ICD}-driven allosteric control. To directly test this mechanism, we examined the E396A mutant, which abolishes Ca_{ICD} binding and locks TRPM4 in the cold-like conformation regardless of temperature[10]. Remarkably, NC1 still produced strong, temperature-independent activation in this mutant, confirming that NC1 does not require the ICD–TMD regulation (Extended Data Fig. 3c). This unprecedented mode of action reveals an alternative allosteric pathway within TRPM4 and highlights NC1 as a promising scaffold for therapeutic development, particularly under conditions where intracellular Ca^{2+} fluctuates.

NBA and CBA inhibit TRPM4 through the S1–S4$_{Lower}$ site

Pharmacological inhibition of TRPM4 is of broad clinical importance, as channel overactivation contributes to arrhythmogenic cardiac disorders, ischemic injury, and cancer progression[18,21,38]. However, our previous work revealed that the endogenous antagonist ATP markedly loses potency at physiological temperature because its binding location shifts between the cold and warm conformations of the channel[10]. This temperature sensitivity limits ATP's ability to suppress TRPM4 under normal cellular conditions[39].

To identify inhibitors that remain effective within the physiological conformational landscape, we turned to NBA and its analog CBA[37]. In contrast to ATP and other temperature-sensitive ligands, NBA and CBA inhibit TRPM4 in a temperature-independent manner,

305 maintaining high potency at 37°C (Extended Data Fig. 2a). This makes them ideal probes for
306 uncovering how TRPM4 inhibition can be achieved under physiological conditions through a
307 temperature-insensitive mechanism.

308 At 37 °C in the presence of Ca^{2+}, cryo-EM analysis of TRPM4 in complex with NBA or CBA
309 uncovered a previously unknown ligand binding site within the S1–S4 domain in both datasets,
310 present in both cold and warm conformations (Extended Data Figs. 6,9). This site lies below the
311 Ca_{TMD} site and adjacent to the S1–$S4_{Upper}$ pocket that accommodates TPPO and NC1, and is
312 therefore termed S1–$S4_{Lower}$ site (Fig. 5a,b). The ligand densities were of excellent quality (local
313 resolution ~2.6 Å) and matched the chemical structures of NBA and CBA, respectively, allowing
314 unambiguous ligand placement (Extended Data Figs. 6; 10a,b; Extended Data Tables 2, 3). In
315 both inhibitors, the chlorophenyl-carboxyl group points upward within the S1–S4 domain, with
316 its carbonyl stabilized by two positively charged residues, R905 on S4 and R1072 on the TRP
317 helix (Fig. 5a,b).

318 Surprisingly, this S1–$S4_{Lower}$ site differs from the NBA binding site previously reported based
319 on lower-resolution cryo-EM maps[40], which placed the inhibitor ~10 Å away on the opposite
320 face of the S4 helix (Extended Data Fig. 10c)—within the cleft between the S1–S4 domain and
321 the pore domain (Extended Data Fig. 10d), analogous to the vanilloid pocket in TRPV channels
322 and the NDNA site in TRPM5[41,42]. Careful inspection of both regions in our high-resolution
323 maps revealed no evidence supporting that earlier assignment. Instead, in our NBA- and CBA-
324 bound structures, the vanilloid pocket consistently displayed the same Y-shaped density seen in
325 apo, TPPO-, and NC1-bound structures, indicating a tightly bound endogenous lipid rather than
326 inhibitor occupancy (Extended Data Fig. 10e).

327 To validate the S1–$S4_{Lower}$ pocket functionally, we introduced mutations at key interacting
328 residues and examined their effects using patch-clamp recordings. Substitution of either R905 or
329 R1072 by alanine completely abolished inhibition (Fig. 5c,d). Moreover, the second aromatic
330 group, a chlorophenyl in CBA or the bulkier naphthyl in NBA, extends downward into a cavity
331 formed between the S4–S5 linker and the TRP helix (Fig. 5a,b). Mutation of Q1061, positioned
332 near this distal aromatic moiety, also markedly reduced inhibition (Fig. 5c,d).

333 Together, these results establish the S1–$S4_{Lower}$ pocket as the functional binding site for NBA
334 and CBA, defining a second pharmacologically active locus within the S1–S4 domain. This

335 domain thus emerges as a bifunctional pharmacological hub of TRPM4, accommodating
336 both activators (TPPO, NC1, Ca^{2+}) and inhibitors (NBA, CBA) through spatially segregated
337 upper and lower sites that converge on shared gating residues such as R1072 on the TRP helix
338 (Fig. 5e).

339 **NBA and CBA inhibit TRPM4 by locking a pre-open conformation**

340 To elucidate how NBA and CBA inhibit Ca^{2+}-dependent activation, we first examined the
341 conformational transitions that underlie canonical TRPM4 gating. In the Ca^{2+}-free cold state,
342 W864 on S3 and H908 on S4 form a stabilizing π–π stacking interaction[43-45]. Upon Ca^{2+} binding,
343 coordinated engagement of the Ca_{TMD} and Ca_{ICD} triggers rearrangements in the S1–S4 bundle
344 and TRP helix, repositioning W864 and H908 and thereby disrupting the contact between the
345 intracellular tips of the S3 and S4 helices (Fig. 5f, the gray structure)—a hallmark of Ca^{2+}-gated
346 TRPM channel activation[42,46]. This frees the S4–S5 linker, allowing the S5–S6 pore domain to
347 open[10].

348 In the Ca^{2+}/NBA- and Ca^{2+}/CBA-bound structures, this transition is blocked. The distal
349 aromatic moiety of NBA or CBA occupies the position normally adopted by H908 in the
350 activated state, thereby forcing H908 to remain in its apo-like conformation. As a result, H908,
351 W864, and the ligand form a π–π–π triple stacking interaction that restrains the S4–S5 linker and
352 prevents pore opening (Fig. 5f, the purple structure). The overall architecture of the inhibited
353 state closely matches the Ca^{2+}-bound warm closed conformation (backbone RMSD 0.7 Å),
354 indicating that NBA and CBA trap TRPM4 in a Ca^{2+}-primed but non-conductive pre-open state.

355 If this model were correct, NBA and CBA should prevent the transition to the fully open state
356 normally induced by positive modulators such as DVT[10,47]. To test this, we determined the
357 structure of TRPM4 in the presence of Ca^{2+}, DVT, and CBA at 37 °C (Extended Data Figs.
358 6,11a; Extended Data Table 3). The resulting map contained densities only for Ca^{2+} and CBA,
359 with no evidence of DVT binding, and the protein conformation was identical to the Ca^{2+}/CBA-
360 bound closed state (Extended Data Fig. 11b). These data provide direct structural evidence that
361 DVT cannot override NBA/CBA inhibition, therefore supporting our hypothesis.

362 Interestingly, this mechanism converges with that of ATP, which also prevents opening by
363 stabilizing the pre-open state, albeit through a distinct intracellular binding site[10]. Unlike ATP,

however, NBA and CBA act from the extracellular side and maintain high potency at physiological temperature, offering both accessibility and stability within the native conformational landscape. Thus, NBA and CBA represent promising scaffolds for the design of TRPM4 inhibitors with therapeutic potential.

Discussion

This study reveals that protein pharmacology is not static but dynamically shaped by the physiological environment, with temperature and intracellular Ca^{2+} acting as active determinants of ligand binding, efficacy and mechanism. By integrating single-particle cryo-EM and electrophysiology, we reveal that these intrinsic factors cooperatively remodel the conformational landscape of TRPM4, exposing latent binding sites and revealing context-dependent pharmacological behaviors that are obscured under non-physiological conditions.

Physiological context unmasks the true pharmacological profiles of ligands. The small molecule TPPO, long regarded as a TRPM5-specific inhibitor, emerges here as a potent activator of TRPM4, but only when both temperature and intracellular Ca^{2+} reach physiological levels (Fig. 6a). Conversely, NC1, previously characterized as a Ca^{2+}-independent agonist, undergoes a functional reversal: at basal Ca^{2+} it activates TRPM4, whereas at elevated Ca^{2+} it becomes antagonized, revealing an unexpected inhibitory facet of Ca^{2+} regulation (Fig. 6b). Mechanistically, these contrasting behaviors arise because temperature and Ca^{2+} cooperatively determine the equilibrium between cold and warm conformations of TRPM4, thereby governing access to key residues within the S1–S4 regulatory domain. Thus, ligand efficacy in TRPM4 is not an intrinsic property of the compound alone, but an emergent consequence of its interplay with the conformational and thermodynamic landscape of the channel.

Moreover, our structural analyses establish the S1–S4 domain as a versatile pharmacological hub that integrates both environmental and chemical inputs. Within this domain, around the Ca_{TMD} site, two spatially distinct but functionally coupled sites control opposite gating outcomes: the S1–$S4_{Upper}$ pocket, occupied by activators TPPO, NC1, and deacetyl bisacodyl[25]; and the S1–$S4_{Lower}$ pocket, targeted by inhibitors NBA and CBA (Fig. 5e). Both pockets converge on the TRP helix through the conserved residue like R1072 on the TRP helix, which serves as a central allosteric node linking environmental cues to gating transitions. Ligand engagement at the upper pocket promotes activation by coupling between the S1–S4 domain and the pore domain,

394 whereas ligand binding to the lower pocket disrupts this coupling, stabilizing a non-conductive
395 state. This dual-site organization provides a unified explanation for how temperature, Ca^{2+} and
396 chemically diverse ligands—activators and inhibitors alike—modulate TRPM4 through a shared
397 structural framework.

398 This regulatory logic uncovered here may represent a general feature of TPRM channels. In
399 TRPM3, both agonists and antagonists occupy the upper pocket[48,49]; and in TRPM8, ligands
400 engage both[50-52]. The S1–S4 domain thus exemplifies an evolutionary design in which
401 temperature and chemical cues dynamically reconfigure a common structural scaffold to yield
402 distinct, context-dependent functional outcomes.

403 Notably, we found that temperature-dependent ligand recognition in TRPM4 is not limited to
404 regions that undergo large-scale rearrangements. Even sites within structurally stable domains—
405 such as the S1–S4 transmembrane bundle, which exhibits only subtle temperature-driven
406 movements—can undergo marked shifts in ligand accessibility and efficacy. This principle likely
407 extends to many drug targets, highlighting that seemingly rigid structural regions may harbor
408 cryptic, environment-sensitive pharmacology.

409 More broadly, these findings advocate for an environment-aware framework of
410 pharmacology. Temperature and intracellular Ca^{2+} are not passive background factors but active
411 regulators that reshape ligand binding, potency, and efficacy. The discrepancy between in vitro
412 screening and in in vivo performance may arise from ignoring such physiological modulators,
413 which can redefine both the apparent selectivity and the mechanism of drug action. By revealing
414 how intrinsic cofactors govern the accessibility and stability of ligand-binding pockets, TRPM4
415 highlights a general principle: pharmacological specificity emerges from the interplay between
416 ligand chemistry and the dynamic structural state of the target protein.

417 For ubiquitously expressed proteins such as TRPM4, these principles carry important therapeutic
418 implications. By exploiting local physiological changes—such as elevated intracellular Ca^{2+}
419 during stress or altered thermal states in disease—future drugs could be tailored to act selectively
420 in pathological contexts while sparing normal function. Such environment-sensitive design
421 strategies may reduce side effects and offer a new route toward precision pharmacology.

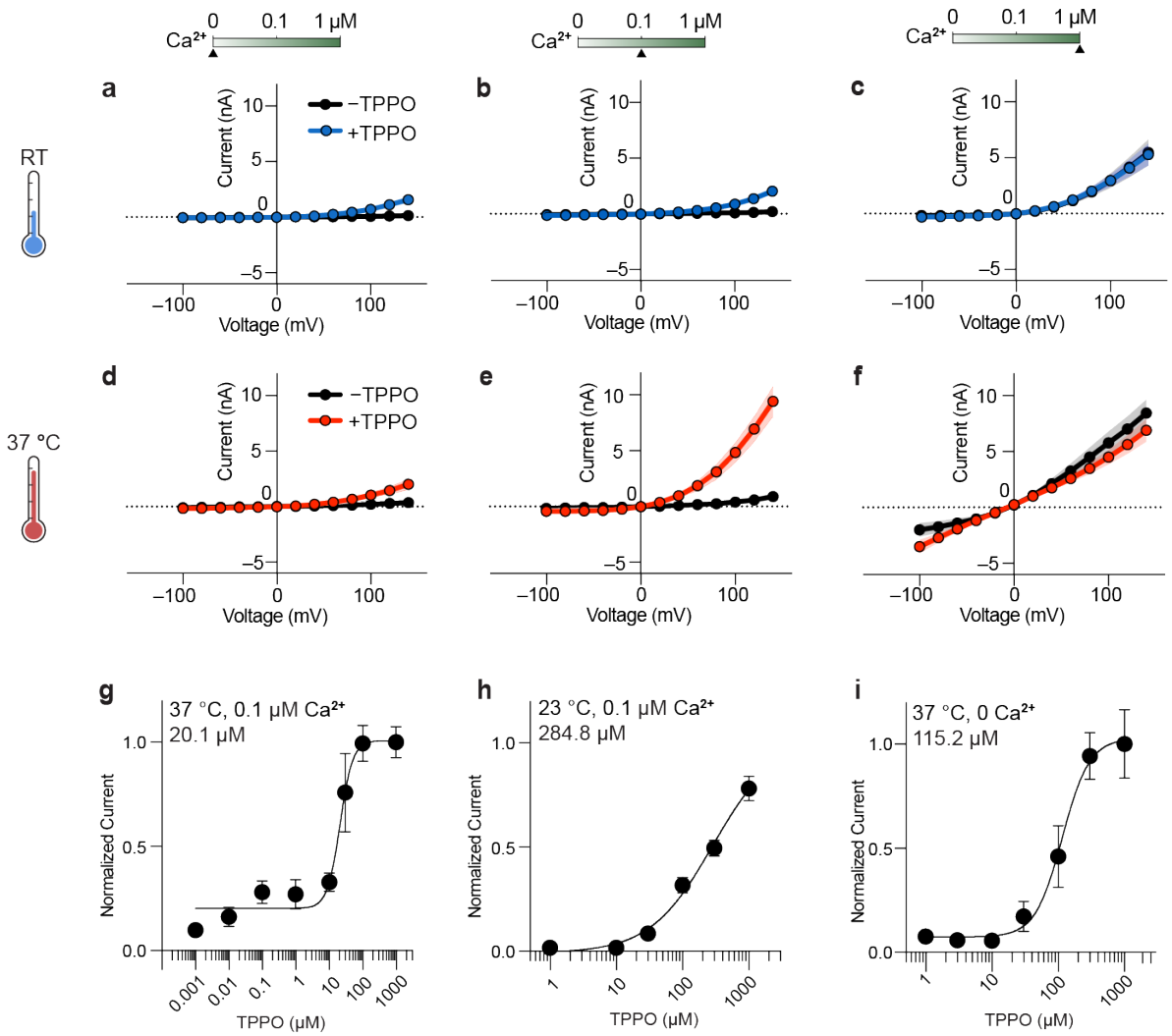

Figure 1. Three-way synergy between TPPO, temperature and Ca^{2+}.

a–f, Whole-cell currents measured in tsA cells overexpressing wild-type TRPM4 at 22 °C (upper panels) and 37 °C (lower panels), with free intracellular Ca^{2+} concentrations of 0 μM (**a, d**), 0.1 μM (**b, e**) and 1 μM (**c, f**), in the presence of 50 μM extracellular TPPO. A voltage protocol stepping from −100 mV to +140 mV in 20-mV increments was applied, with each voltage step lasting 100 ms. The currents from all measured cells were then averaged and plotted versus voltage to generate the mean I–V curve, with the line representing the mean and the shaded indicating the s.e.m. The numbers of independently measured cells are as follows: (**a**) n=9 (−TPPO) / 9 (+TPPO), (**b**) n=7 (−TPPO) / 8 (+TPPO), (**c**) n=9 (−TPPO) / 9 (+TPPO), (**d**) n=7 (−TPPO) / 10 (+TPPO), (**e**) n=8 (−TPPO) / 8 (+TPPO), and (**f**) n=6 (−TPPO) / 6 (+TPPO). **g–i**,

433 TPPO dose-response measurements for wild-type TRPM4 with 0.1 μM free intracellular Ca^{2+} at
434 37 °C (**g**), 0.1 μM Ca^{2+} at 23 °C (**h**), and 0 μM Ca^{2+} at 37 °C (**i**). A voltage protocol was applied
435 every 10 s to monitor current changes: –100 mV for 200 ms, followed by +100 mV for 200 ms.
436 Once the current stabilized at each TPPO concentration, the current amplitudes at +100 mV from
437 all measured cells were averaged, and the mean amplitudes were plotted and fitted to obtain the
438 EC_{50}. Current amplitudes were normalized either to the mean at 1000 μM TPPO (**g, i**) or to the
439 fitted I_max from the Hill equation (**h**). Data are presented as mean ± s.e.m. The numbers of
440 independently measured cell are as follows: (**g**) n=7 for all concentrations, (**h**) n=5 at 1 μM and
441 n=7 for all other concentrations, and (**i**) n=7 for all concentrations.

442

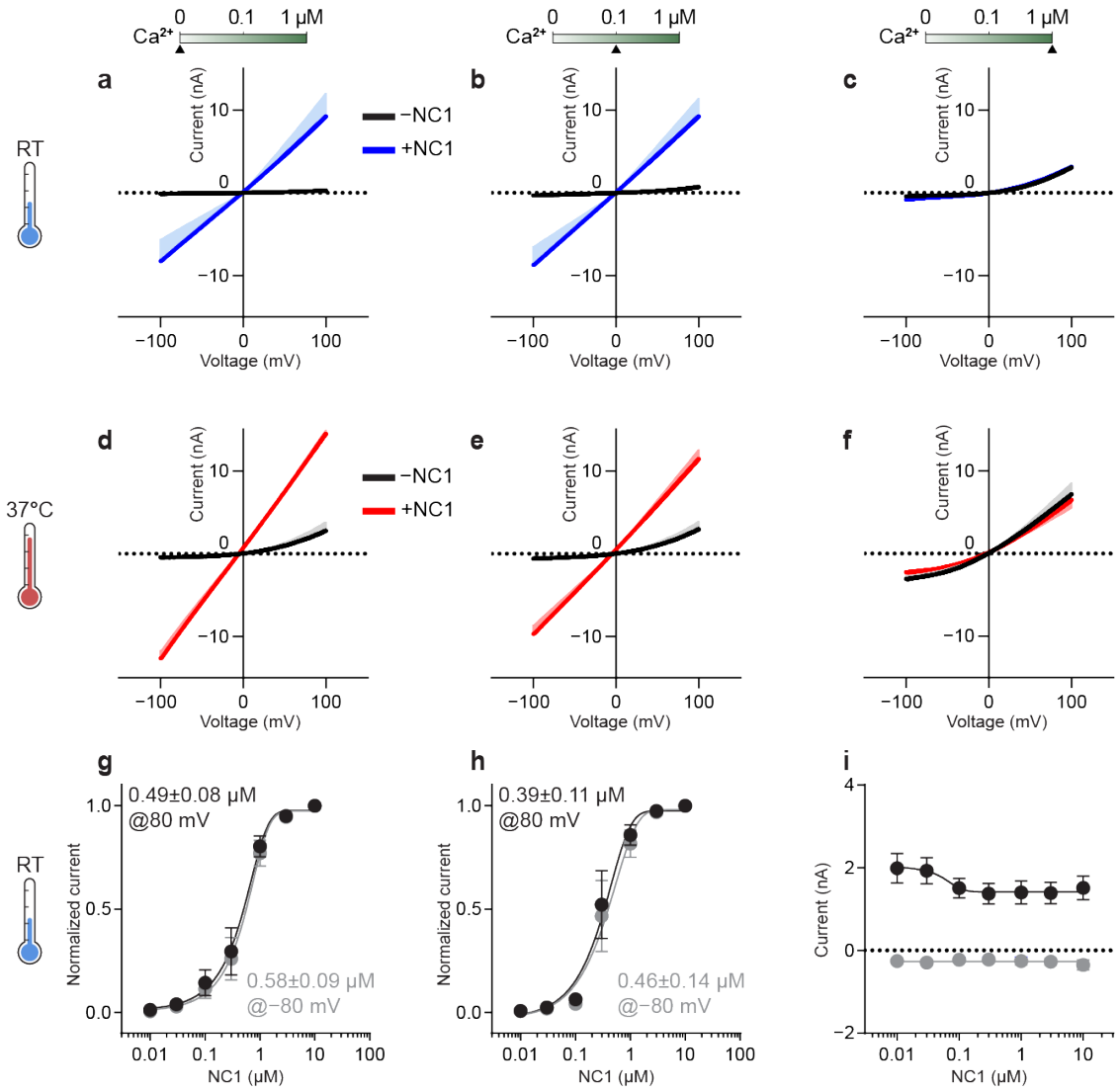

Figure 2. Ca^{2+}-dependent gating reversal of NC1.

a–f, Whole-cell currents measured in tsA cells overexpressing wild-type TRPM4 at 22 °C (upper panels) and 37 °C (lower panels), with free intracellular Ca^{2+} concentrations of 0 μM (**a, d**), 0.1 μM (**b, e**) and 1 μM (**c, f**). A voltage protocol was applied every 5 s to monitor current changes until reaching steady state: −100 mV for 50 ms, ramped to +100 mV over 200 ms and held at +100 mV for 50 ms. The currents without and with 1 μM extracellular NC1 in each condition were measured in a single cell. The currents from all measured cells were then averaged and plotted versus voltage to generate the mean I–V curve, with the line representing the mean and the shaded indicating the s.e.m. For clarity, the s.e.m. envelope was plotted in one direction. The numbers of independently measured cells are as follows: n=5 (**a**), n=7 (**b**), n=5 (**c**), n=5 (**d**), n=4

454 (**e**), and n=4 (**f**). **g–i**, NC1 dose-response measurements for wild-type TRPM4 at
455 22 °C with 0 μM free intracellular Ca^{2+} (**g**), 0.1 μM Ca^{2+} (**h**), and 1 μM Ca^{2+} (**i**). A voltage
456 protocol was applied every 5 s to monitor current changes: 0 mV for 50 ms, switch to +80 mV
457 for 50 ms, followed by −80 mV for 50 ms, and return to 0 mV for 50 ms. Once the current
458 stabilized at each NC1 concentration, the current amplitudes at +80 mV and −80 mV were
459 normalized to those at 10 μM NC1. Normalized currents from all measured cells were averaged
460 and plotted as mean ± s.e.m. EC_{50} values obtained from individual cells were averaged to yield
461 the final EC_{50} reported as mean ± s.e.m. (**g**,**h**). Data are presented as mean ± s.e.m. The numbers
462 of independently measured cells are as follows: n=5 (**g**), n=5 (**h**), and n=4 (**i**).

463

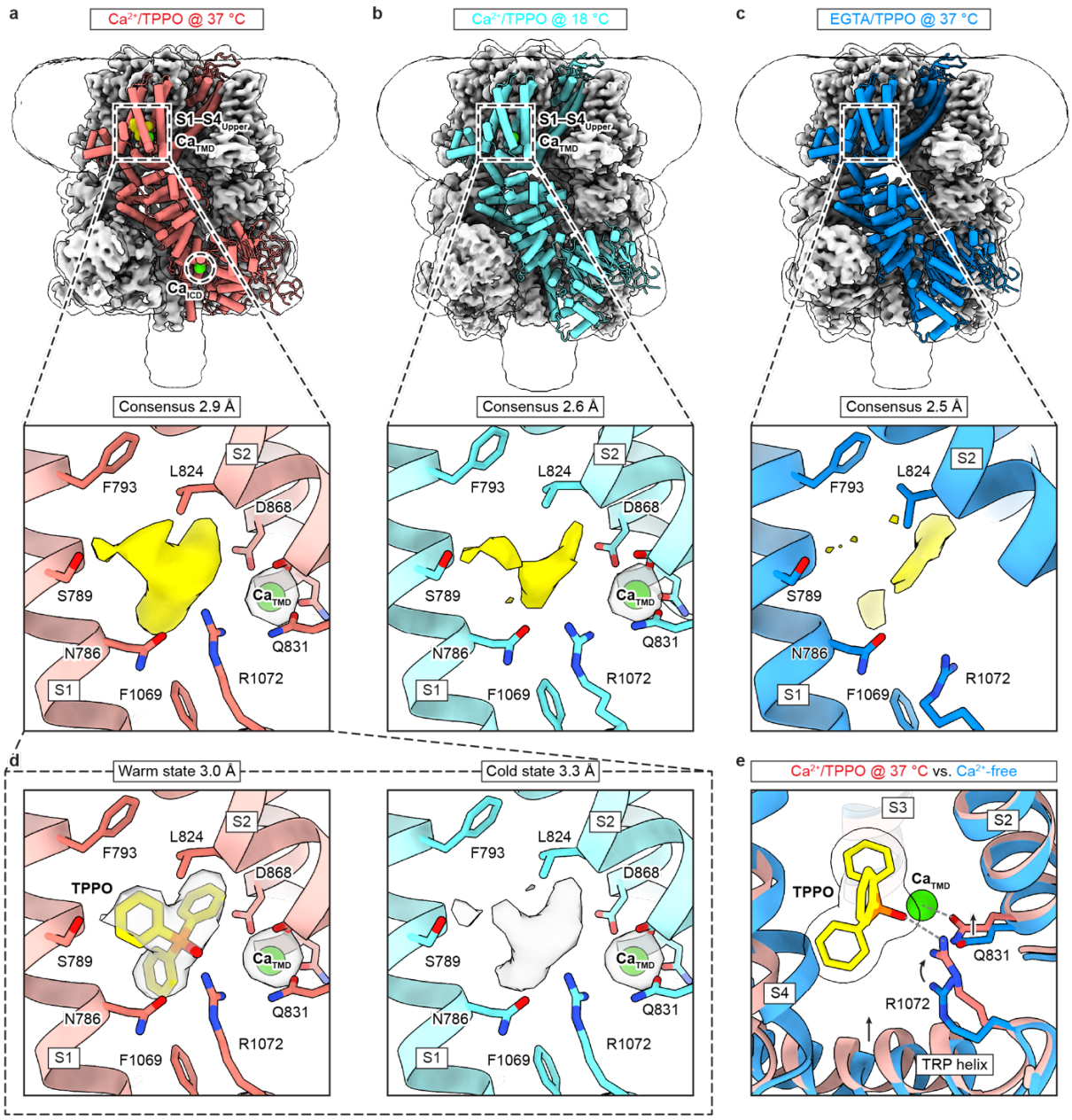

464

465 **Figure 3. Structural basis of the three-way synergy between TPPO, temperature and Ca^{2+}.**

466 **a–c**, Structures of TRPM4 in complex with Ca^{2+}/TPPO at 37 °C (**a**, PDB-ID 9Z1W), Ca^{2+}/TPPO
467 at 18 °C (**b**, PDB-ID 9Z1Z), and EGTA/TPPO at 37 °C (**c**, PDB-ID 9Z20). One subunit is shown
468 in cartoon representation, while the remaining three subunits are displayed as the cryo-EM map,
469 viewed parallel to the membrane. The transparent envelope outlines the detergent micelle and the
470 disordered region of the C-terminal coiled-coil. TPPO is highlighted in yellow and Ca^{2+} in green.
471 The resolution of the consensus map is indicated below. Bottom panels show the details of the

S1–S4 binding site in the consensus maps. The protein backbone is shown in cartoon representation, with key interacting residues in stick representation. Densities at the TPPO binding site (yellow) and at the Ca_{TMD} site (transparent in **a**,**b**) are contoured at 4.5 σ. **d**, Details of the S1–S4 binding site in the warm (left, PDB-ID 9Z1X) and cold (right, PDB-ID 9Z1Y) states, obtained from classification of the Ca^{2+}/TPPO dataset collected at 37 °C. The resolution of each cryo-EM map is indicated. Densities at the TPPO binding site and the Ca_{TMD} site are shown as transparent surface representations contoured at 9 σ. The fitted TPPO molecule is shown in stick representation (only in the warm state), and Ca_{TMD} as a green sphere. **e**, Structural comparison of TRPM4 with Ca^{2+}/TPPO at 37 °C (salmon, PDB-ID 9Z1X) and the Ca^{2+}-free apo state (blue, PDB-ID 9B93), superimposed using the S1–S4 (residues 760–910). TPPO is shown in stick representation with a transparent envelope, and Ca_{TMD} as a green sphere. Black arrows indicate the approximate direction of movement of key residues and the TRP helix. The dashed lines mark key interactions.

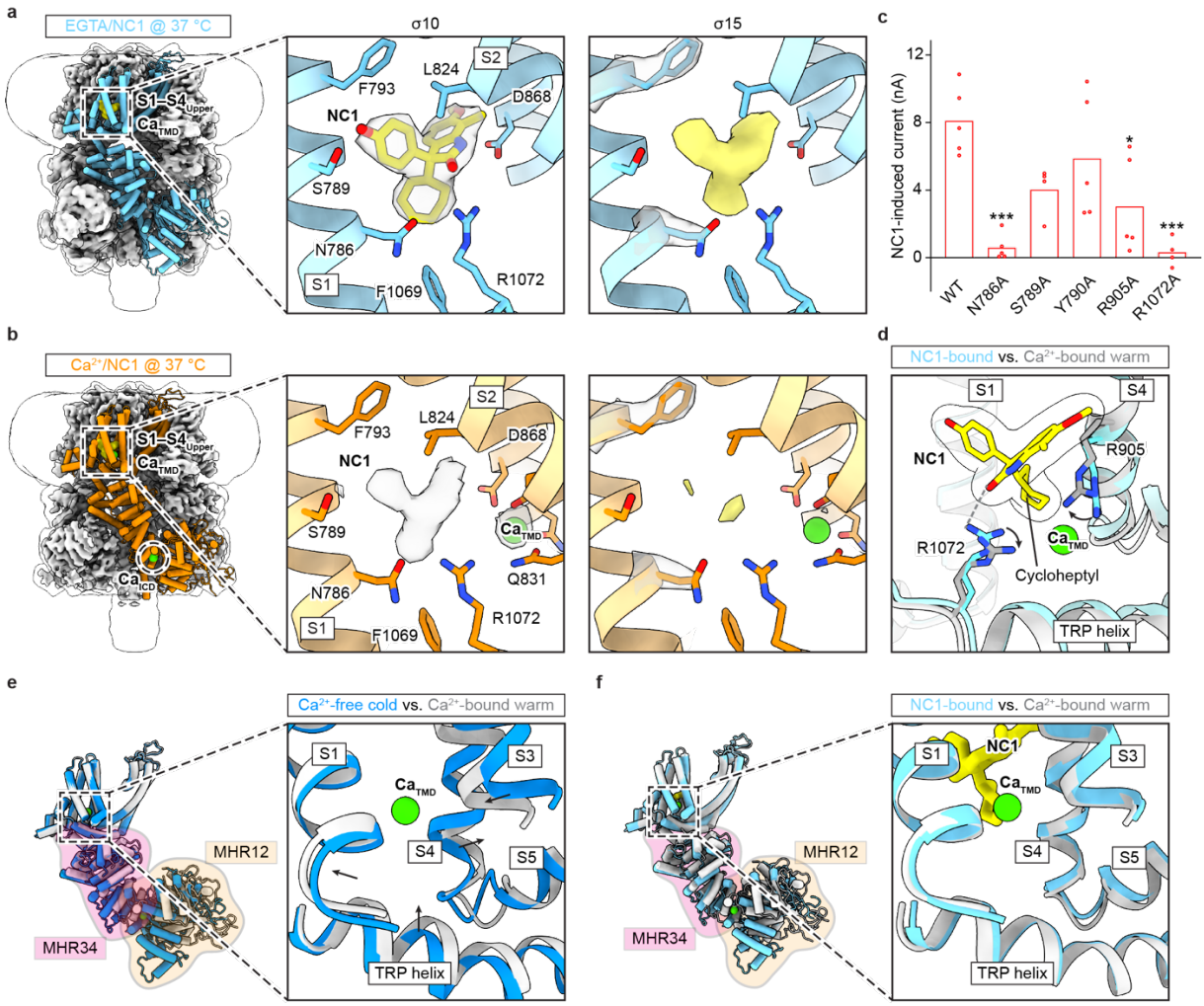

Figure 4. Mechanistic basis for Ca^{2+}-dependent gating reversal of NC1.

a,**b** The left panels show the structures of TRPM4 in complex with EGTA/NC1 at 37 °C (**a**, PDB-ID 9Z22) and Ca^{2+}/NC1 at 37 °C (**b**, PDB-ID 9Z21). One subunit is shown in cartoon representation, while the remaining three subunits are displayed as the cryo-EM map, viewed parallel to the membrane. The transparent envelope outlines the detergent micelle and the disordered region of the C-terminal coiled-coil. The middle panels show the details of the S1–S4 binding site, with the protein backbone in cartoon representation and key interacting residues in stick representation. Densities at the NC1 binding site, and at the Ca_{TMD} site (only in **b**) are shown as transparent surface representations contoured at 10 σ. The fitted NC1 molecule in (only in **a**) is shown in stick representation, and Ca_{TMD} as a green sphere (only in **b**). The right panels present the same regions as the middle panels but additionally display densities for well-defined

498 side chains within the binding site, contoured at 15 σ. **c**, NC1-induced whole-cell current
499 amplitudes at +100 mV in cells overexpressing wild-type TRPM4 and binding-site mutants,
500 calculated by subtracting the steady-state current recorded before NC1 application from that
501 recorded after application. Each point represents an independently measured cell (n = 5 (WT), 5
502 (N786A), 4 (S789A), 5 (Y790A), 5 (R905A), 4 (R1072A)), with bars indicating the
503 mean. Statistical analysis was performed using one-way ANOVA with Bonferroni's post hoc test,
504 comparing each mutant with wild type (*$p<0.05$, ***$p<0.001$). Averaged raw data are shown in
505 Extended Data Fig. 3b. **d**, Structural comparison of TRPM4 NC1-bound state (cyan, PDB-ID
506 9Z22) and the Ca^{2+}-bound warm state (blue, PDB-ID 9B8W) of TRPM4, superimposed using the
507 S1–S4 (residues 760–910). NC1 is shown in stick representation with a transparent envelope,
508 and Ca_{TMD} as a green sphere. Black arrows indicate the approximate direction of movement of
509 key residues. The dashed line marks a key interaction. **e**, Structural comparison of a single
510 subunit of the Ca^{2+}-free cold state (blue, PDB-ID 9B93) and the Ca^{2+}-bound warm state (grey,
511 PDB-ID 9B8W) of TRPM4, superimposed using the S1–S4 (residues 760–910). MHR3/4 is
512 outlined with a pink envelope and MHR1/2 with an orange envelope. The right panel shows
513 details of the S1–S4 binding site and its surroundings. Ca_{TMD} is shown in a green sphere, and the
514 black arrows indicate the movement of structural elements forming the binding site upon Ca^{2+}
515 binding. **f**, Structural comparison of the NC1-bound state (cyan, PDB-ID 9Z22) and the Ca^{2+}-
516 bound warm state (grey, PDB-ID 9B8W) of TRPM4. The structures are superimposed and
517 displayed similarly to panel (**e**). NC1 is shown in stick representation, and Ca_{TMD} as a green
518 sphere.

519

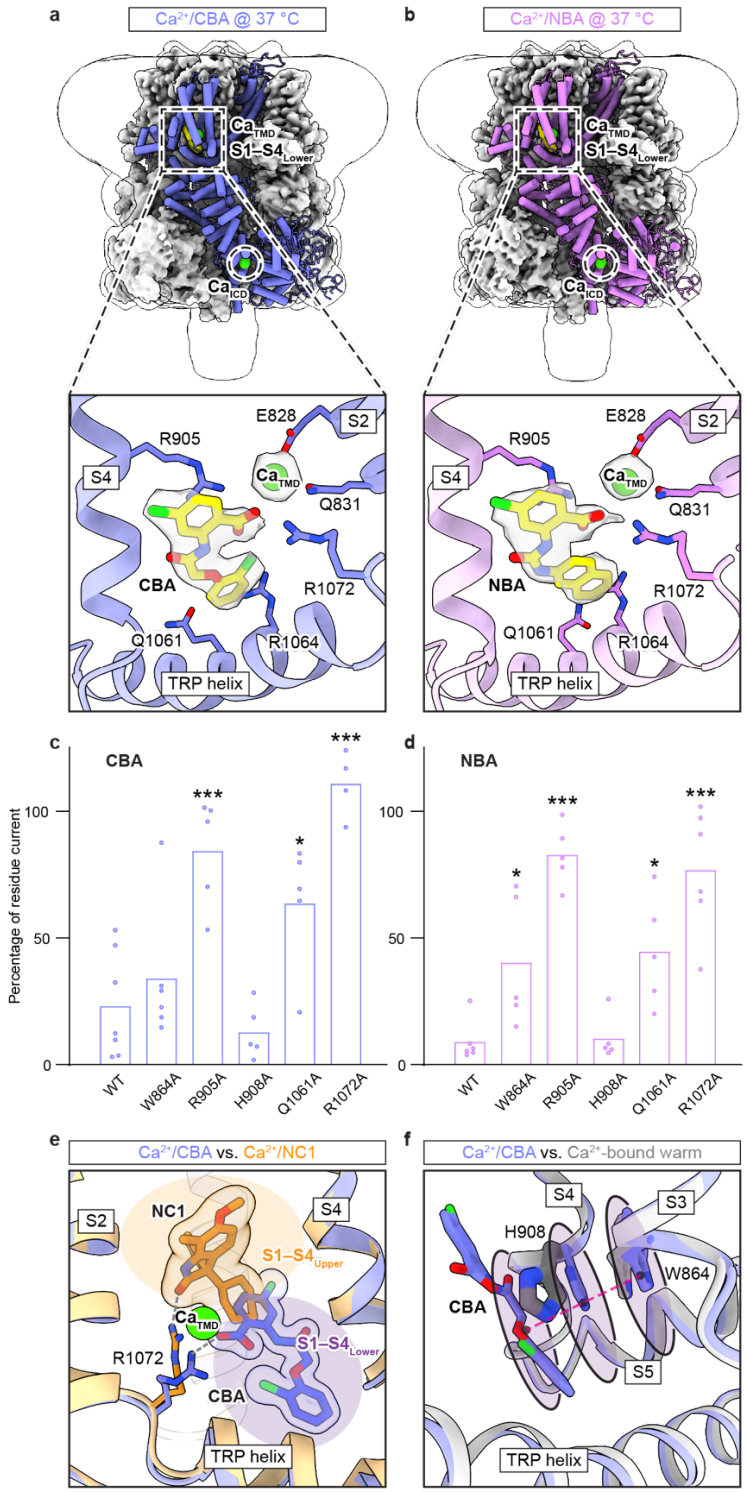

520

521 **Figure 5. NBA and CBA inhibit TRPM4 through the S1–S4$_{Lower}$ site.**

522 **a**,**b** Structure of TRPM4 in complex with Ca^{2+}/CBA at 37 °C (**a**, PDB-ID 9Z23) and Ca^{2+}/NBA
523 at 37 °C (**b**, PDB-ID 9Z25). One subunit is shown in cartoon representation, while the remaining

three subunits are displayed as the cryo-EM map, viewed parallel to the membrane. The transparent envelope outlines the detergent micelle and the disordered region of the C-terminal coiled-coil. CBA and NBA are highlighted in yellow and Ca^{2+} in green. Bottom panels show the details of the S1–S4 binding site, with the protein backbone in cartoon representation and key interacting residues in stick representation. Densities for CBA and Ca_{TMD} (**a**) and for NBA and Ca_{TMD} (**b**) are shown as transparent surface representations contoured at 17 σ and 20 σ, respectively. The fitted CBA and NBA molecules are shown in stick representation, and Ca_{TMD} as a green sphere. **c,d**, CBA- and NBA-dependent inhibition at +100 mV in cells overexpressing wild-type TRPM4 and binding-site mutants. The percentage of remaining currents after the application of NBA or CBA at 22 °C was calculated by dividing the steady-state current recorded after NBA or CBA application by the steady-state current recorded before application. Each point represents an independently measured cell: NBA, n = 6 (WT), 5 (W864A), 5 (R905A), 5 (H908A), 5 (Q1061A), and 6 (R1072A); CBA, n = 7 (WT), 6 (W864A), 5 (R905A), 5 (H908A), 5 (Q1061A), and 4 (R1072A). Bars indicate the mean. Statistical analysis was performed using one-way ANOVA with Bonferroni's post hoc test, comparing each mutant with wild type. (*$p<0.05$, ***$p<0.001$). Averaged raw data are shown in Extended Data Fig. 2b. **e**, Structural comparison of the Ca^{2+}/CBA-bound state (blue, 9Z23) and the NC1-bound state (orange, PDB-ID 9Z21) of TRPM4, superimposed using S1–S4 (residues 760–910). CBA and NC1 are shown in stick representation with a transparent envelope, and Ca_{TMD} as a green sphere. The filled orange and blue ellipses mark the upper and lower pockets within the S1–S4 domain, respectively. Arg1072 interacts with both ligands, as indicated by the dashed lines. **f**, Structural comparison of the Ca^{2+}/CBA-bound state (blue, PDB-ID 9Z23) and the Ca^{2+}-bound warm state (grey, PDB-ID 9B8W) of TRPM4, superimposed using S1–S4 (residues 760–910). CBA and the side chains of H908 and W864 are shown as stick representation, forming a triple stacking interaction indicated by the transparent discs and the red dashed line.

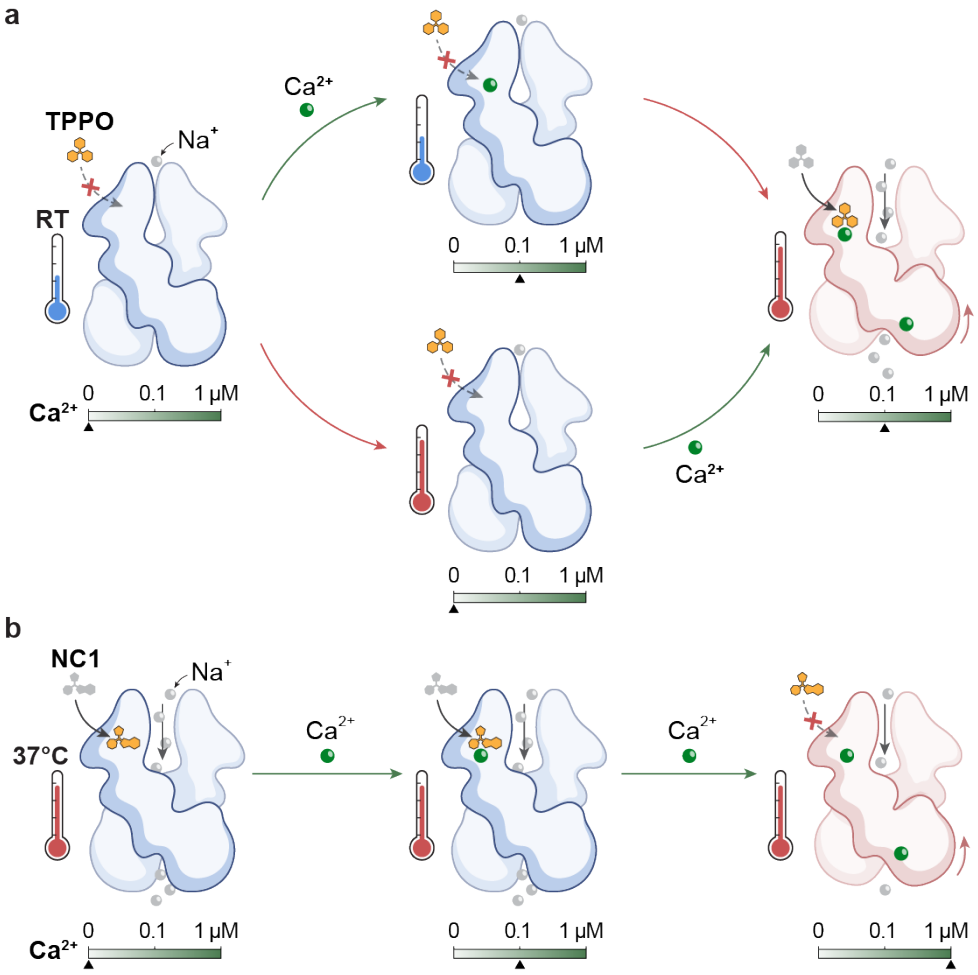

Figure 6. Distinct temperature- and Ca^{2+}-dependent activation mechanisms of TPPO and NC1 on TRPM4.

a, Schematic representation of the polymodal activation of TRPM4 by TPPO, Ca^{2+}, and temperature. Neither resting Ca^{2+} levels nor physiological temperature alone is sufficient to enable TPPO-mediated activation. Only when both resting Ca^{2+} and physiological temperature are present can TPPO exert its activating effect. **b**, Schematic representation of NC1 activity, which functions independently of Ca^{2+} at resting levels but loses efficacy once intracellular Ca^{2+} rises to stimulatory concentrations.

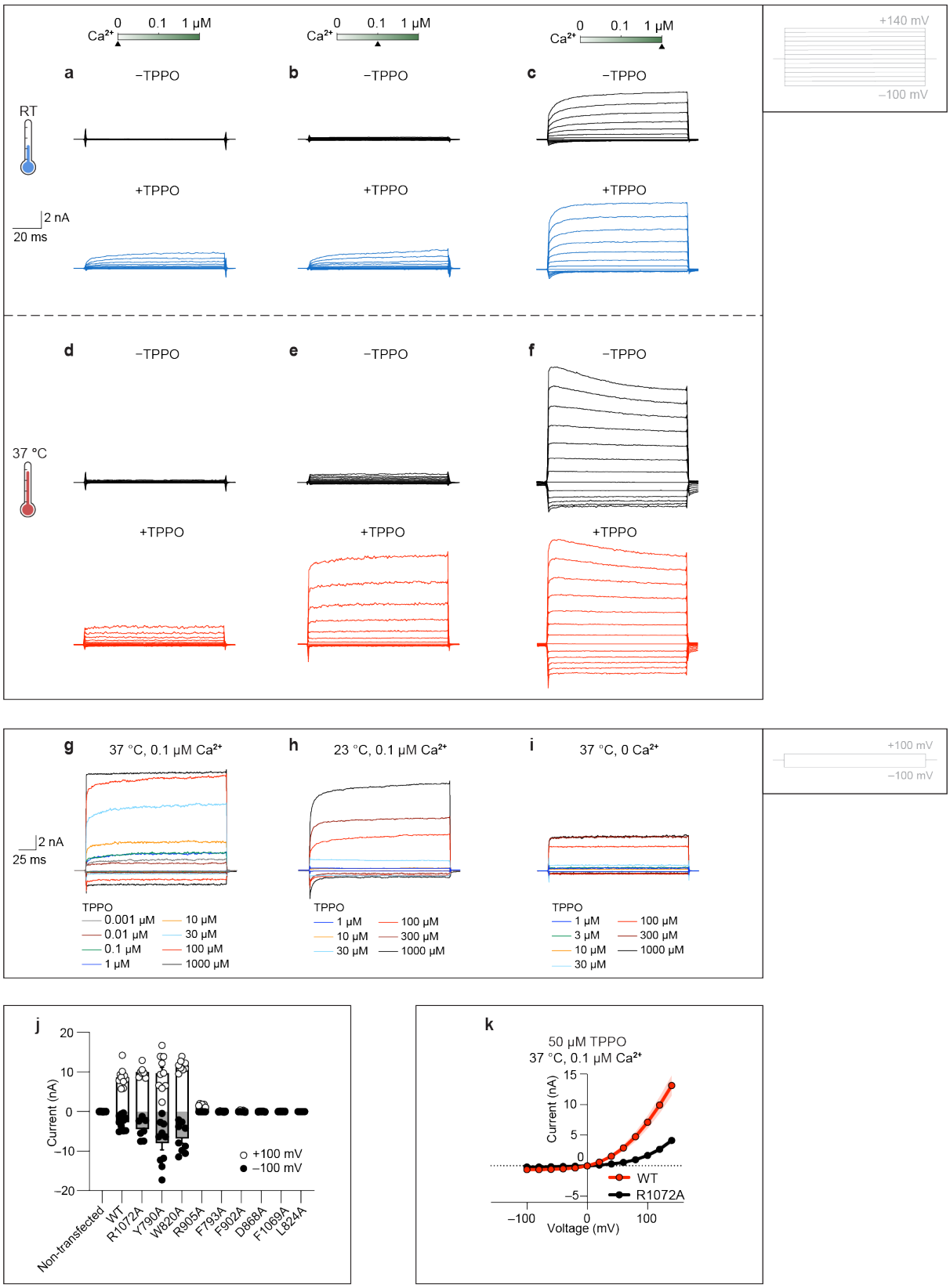
Ca²⁺ 0 0.1 1 μM
a
b
c
−TPPO
+TPPO
RT
2 nA
20 ms
+140 mV
−100 mV
d
e
f
37 °C
g
37 °C, 0.1 μM Ca²⁺
h
23 °C, 0.1 μM Ca²⁺
i
37 °C, 0 Ca²⁺
+100 mV
−100 mV
25 ms
TPPO
0.001 μM
0.01 μM
0.1 μM
1 μM
10 μM
30 μM
100 μM
1000 μM
300 μM
3 μM
j
Current (nA)
+100 mV
−100 mV
Non-transfected
WT
R1072A
Y790A
W820A
R905A
F793A
F902A
D868A
F1069A
L824A
k
50 μM TPPO
37 °C, 0.1 μM Ca²⁺
Current (nA)
Voltage (mV)
WT
R1072A

560

561 **Extended Data Figure 1. Electrophysiological characterization of TPPO-dependent**
562 **activation of TRPM4.**

563 **a–f**, Representative whole-cell current traces recorded at room temperature (23 °C) and 37 °C
564 with free intracellular Ca^{2+} concentrations of 0 μM (**a**,**d**), 0.1 μM (**b**,**e**), and 1 μM (**c**,**f**), evoked
565 by a voltage-step protocol from –100 mV to +140 mV in 20-mV increments (100 ms per step).
566 The currents without and with 50 μM extracellular TPPO at each condition were measured from
567 a single cell. **g–i**, Representative whole-cell current traces from the TPPO dose response
568 recordings acquired using a two-step protocol (–100 mV followed by +100 mV for 200 ms each)
569 under 0.1 μM Ca^{2+} at 37 °C (**g**), 0.1 μM Ca^{2+} at 23 °C (**h**), and 0 μM Ca^{2+} at 37 °C (**i**). **j**, Whole-
570 cell currents of non-transfected tsA cells and tsA cells overexpressing wild-type TRPM4 and
571 TPPO binding-site mutants evoked by 1 μM free intracellular Ca^{2+} and measured at +100 and
572 −100 mV at room temperature. Each point represents an independently measured cell: non-
573 transfected tsA201 (n=8), WT (n=10), R1072A (n=10), Y790A (n=7), W820A (n=10), W828A
574 (n=9), S789A (n=12), R905A (n=7), F793A (n=12), F902A (n=6), D868A (n=5), E898A (n=3),
575 F1069A (n=4), and L824A (n=5). Bars indicate the mean. **k**, Mean I–V relationships from tsA
576 cells overexpressing wild-type TRPM4 or the R1072A mutant under the condition of 0.1 μM free
577 intracellular Ca^{2+} and 50 μM extracellular TPPO, measured at 37 °C. Currents were elicited
578 using a voltage-step protocol from –100 mV to +140 mV. Steady-state currents at each voltage
579 were averaged and plotted (WT, n=15; R1072A, n=10). Data are presented as mean ± s.e.m.

580

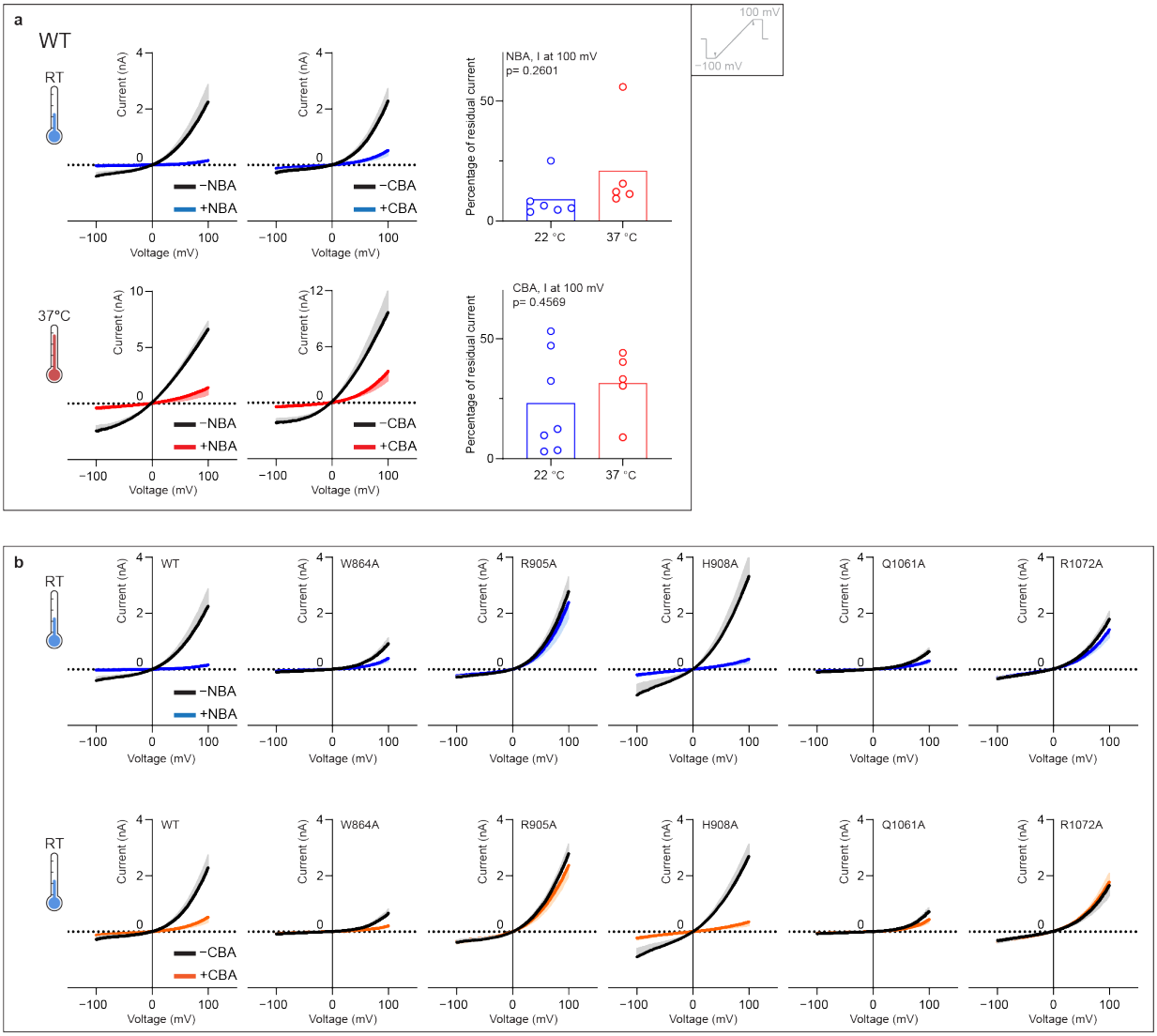

581

582 **Extended Data Figure 2. Electrophysiological characterization of TRPM4 inhibition by**
583 **NBA and CBA.**

584 **a**, Left and middle panels show whole-cell currents measured in tsA cells overexpressing wild-
585 type TRPM4 at 22 °C and 37 °C, with 1 μM free intracellular Ca^{2+}. A voltage protocol was
586 applied every 5 s to monitor current changes until reaching steady state: −100 mV for 50 ms,
587 ramped to +100 mV over 200 ms, and held at +100 mV for 50 ms. The currents without and with
588 10 μM extracellular NBA or CBA at each condition were measured from a single cell. The
589 currents from all measured cells were then averaged and plotted versus voltage to generate the
590 mean I–V curve, with the line representing the mean and the shaded indicating the s.e.m. For
591 clarity, the s.e.m. envelope was plotted in one direction. The numbers of independently measured

592 cells are as follows: n=6 (NBA, 22 °C), n=5 (NBA, 37 °C), n=7 (CBA, 22 °C), n=5 (CBA,
593 37 °C). Right panels show quantification of CBA- and NBA-dependent inhibition at +100 mV
594 for the recordings shown in the left and middle panels. The percentage of remaining currents
595 after the application of NBA or CBA was calculated by dividing the steady-state current recorded
596 after NBA or CBA application by the steady-state current recorded before application. Each
597 point represents an independently measured cell, and bars indicate the mean. A t-test was used to
598 compare inhibition at 22 °C versus 37 °C. **b**, Whole-cell currents measured in tsA cells
599 overexpressing wild-type TRPM4 or NBA/CBA binding-site mutants at 22 °C, with 1 μM free
600 intracellular Ca^{2+}, without and with 10 μM extracellular NBA or CBA. Measurements and
601 analysis were performed as in panel (**a**). The numbers of independently measured cells are as
602 follows. NBA: n=6 (WT), n=6 (W864A), n=5 (R905A), n=5 (H908A), n=6 (Q1061A), n=6
603 (R1072A); CBA: n=7 (WT), n=6 (W864A), n=5 (R905A), n=5 (H908A), n=5 (Q1061A), n=4
604 (R1072A).

605

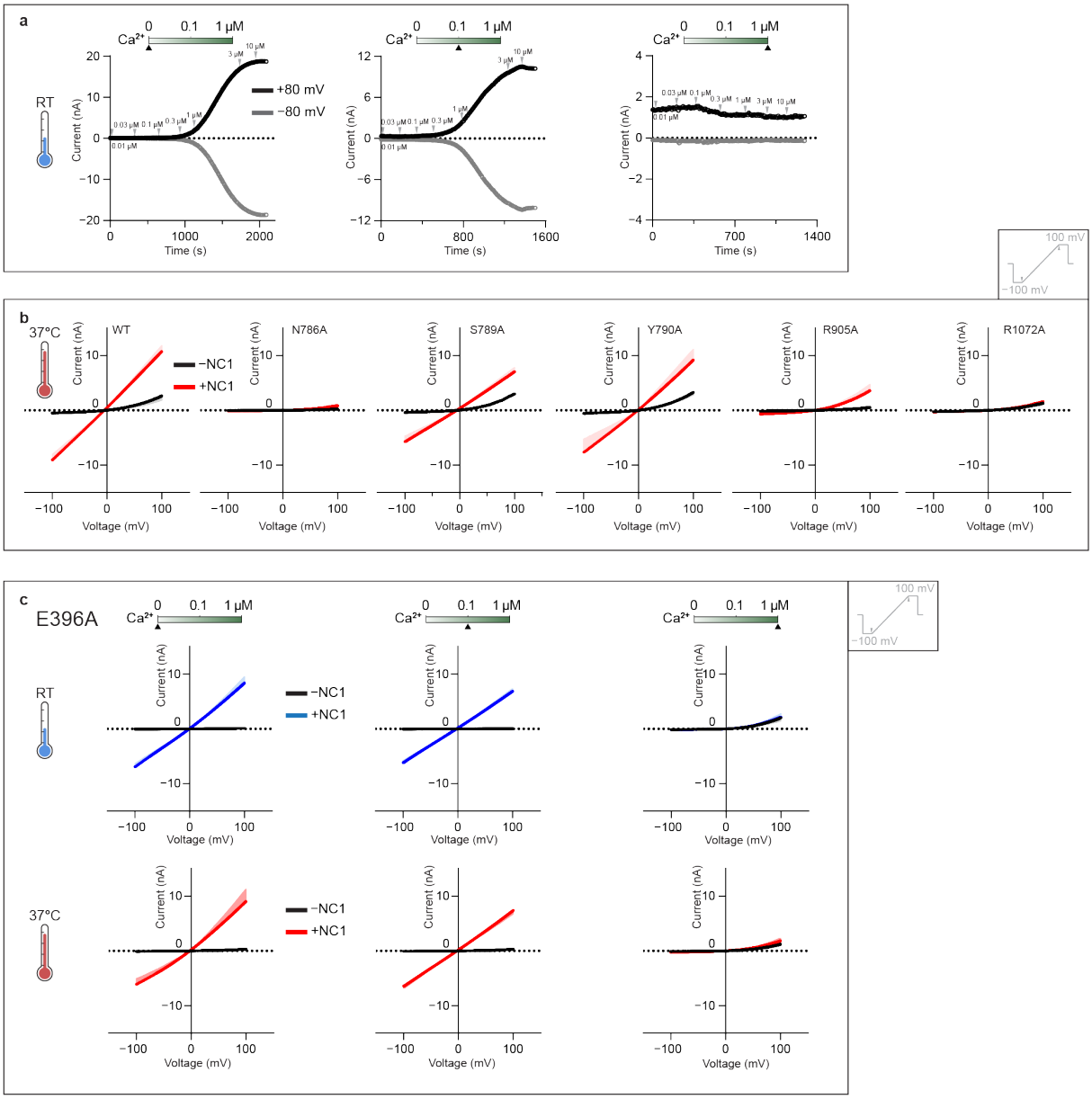

Extended Data Figure 3. Electrophysiological characterization of NC1-dependent activation of TRPM4.

a, The representative current traces for the NC1 dose-response measurements for wild-type TRPM4 at 22 °C with free intracellular Ca^{2+} of 0 μM, 0.1 μM, and 1 μM. A voltage protocol was applied every 5 s to monitor current changes: 0 mV for 50 ms, switch to +80 mV for 50 ms, followed by −80 mV for 50 ms, and return to 0 mV for 50 ms. **b**, Whole-cell currents measured in tsA cells overexpressing wild-type TRPM4 or NC1 binding-site mutants at 37 °C, with 0.1 μM

free intracellular Ca^{2+}, without and with 1 μM extracellular NC1. A voltage protocol was applied every 5 s to monitor current changes until reaching steady state: −100 mV for 50 ms, ramped to +100 mV over 200 ms, and held at +100 mV for 50 ms. The currents without and with NC1 at each condition were measured from a single cell. The currents from all measured cells were then averaged and plotted versus voltage to generate the mean I–V curve, with the line representing the mean and the shaded indicating the s.e.m. For clarity, the s.e.m. envelope was plotted in one direction. The numbers of independently measured cells are as follows: n=5 (WT), n=5 (N786A), n=4 (S789A), n=5 (Y790A), n=5 (R905A), n=4 (R1072A). **c**, Whole-cell currents were measured in tsA cells overexpressing the E396A mutant of TRPM4 at 22 °C (upper panels) and 37 °C (lower panels), with intracellular free Ca^{2+} concentrations of 0 μM, 0.1 μM, and 1 μM. A voltage protocol was applied every 5 s to monitor current changes: −100 mV for 50 ms, ramped to +100 mV over 200 ms and held at +100 mV for 50 ms. The current without or with 1 μM extracellular NC1 in each condition was measured in a single cell. The currents from all measured cells were then averaged and plotted versus voltage to generate the mean I–V curve, with the line representing the mean and the shaded indicating the s.e.m. For clarity, the s.e.m. envelope was plotted in one direction. The numbers of independently measured cells are as follows: n=5 (0 μM Ca^{2+}, 22 °C), n=5 (0.1 μM Ca^{2+}, 22 °C), n=5 (1 μM Ca^{2+}, 22 °C), n=5 (0 μM Ca^{2+}, 37 °C), n=5 (0.1 μM Ca^{2+}, 37 °C) and n=5 (1 μM Ca^{2+}, 37 °C).

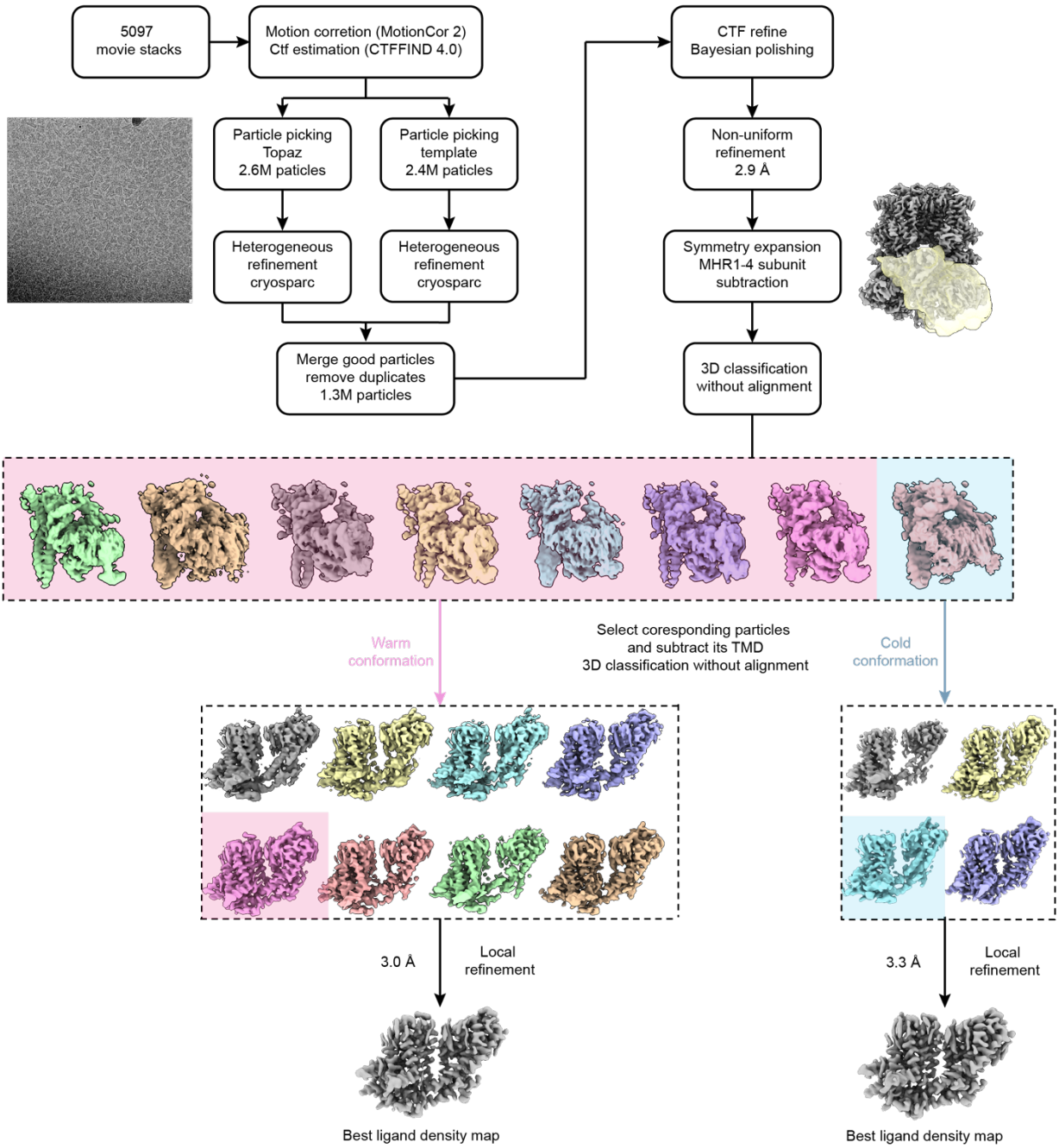

Extended Data Figure 4. Cryo-EM data processing workflow for the Ca^{2+}/TPPO–TRPM4–37 °C dataset. A representative micrograph is shown. The final consensus map and the TMD-focused map with the best-resolved ligand density are displayed with their respective resolutions.

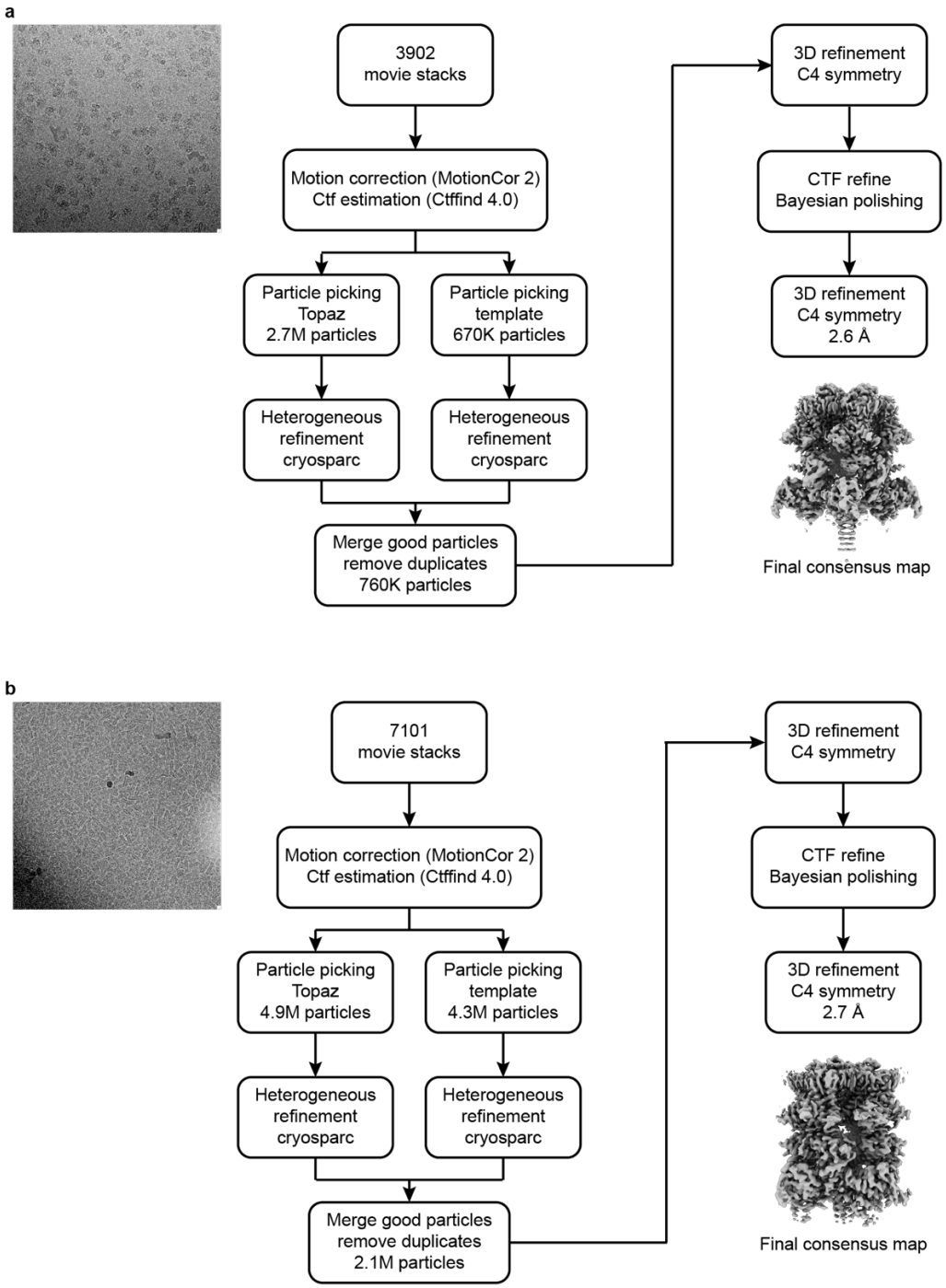

Extended Data Figure 5. Cryo-EM data processing workflow for the Ca^{2+}/TPPO–TRPM4–18 °C (a) and EGTA/TPPO–TRPM4–37 °C (b) datasets. Representative micrographs are shown. The final maps are displayed with their respective resolutions.

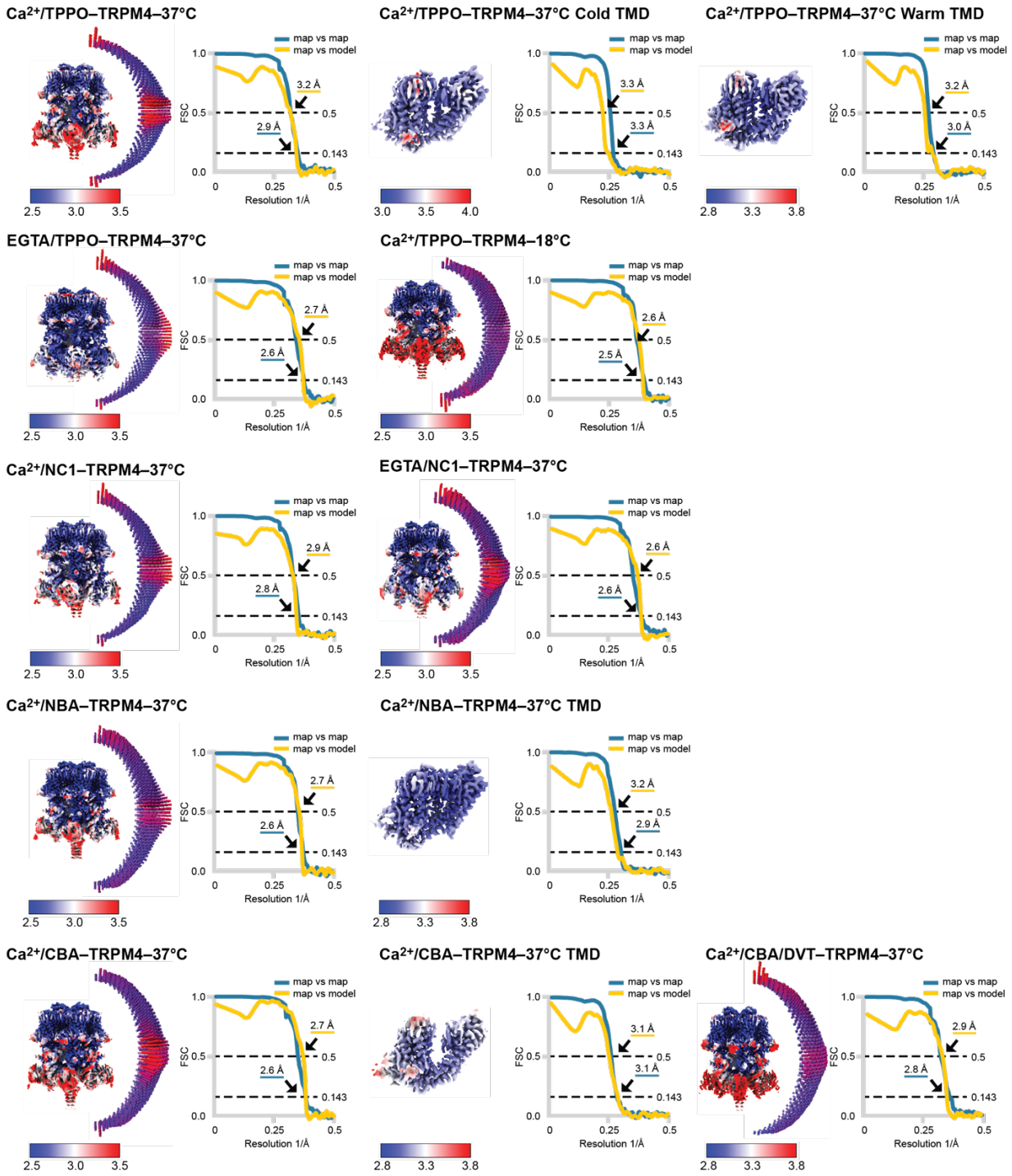

Extended Data Figure 6. Assessment of cryo-EM data quality. For each map, left: cryo-EM maps colored by local resolution; right: Fourier shell correlation (FSC) plot.

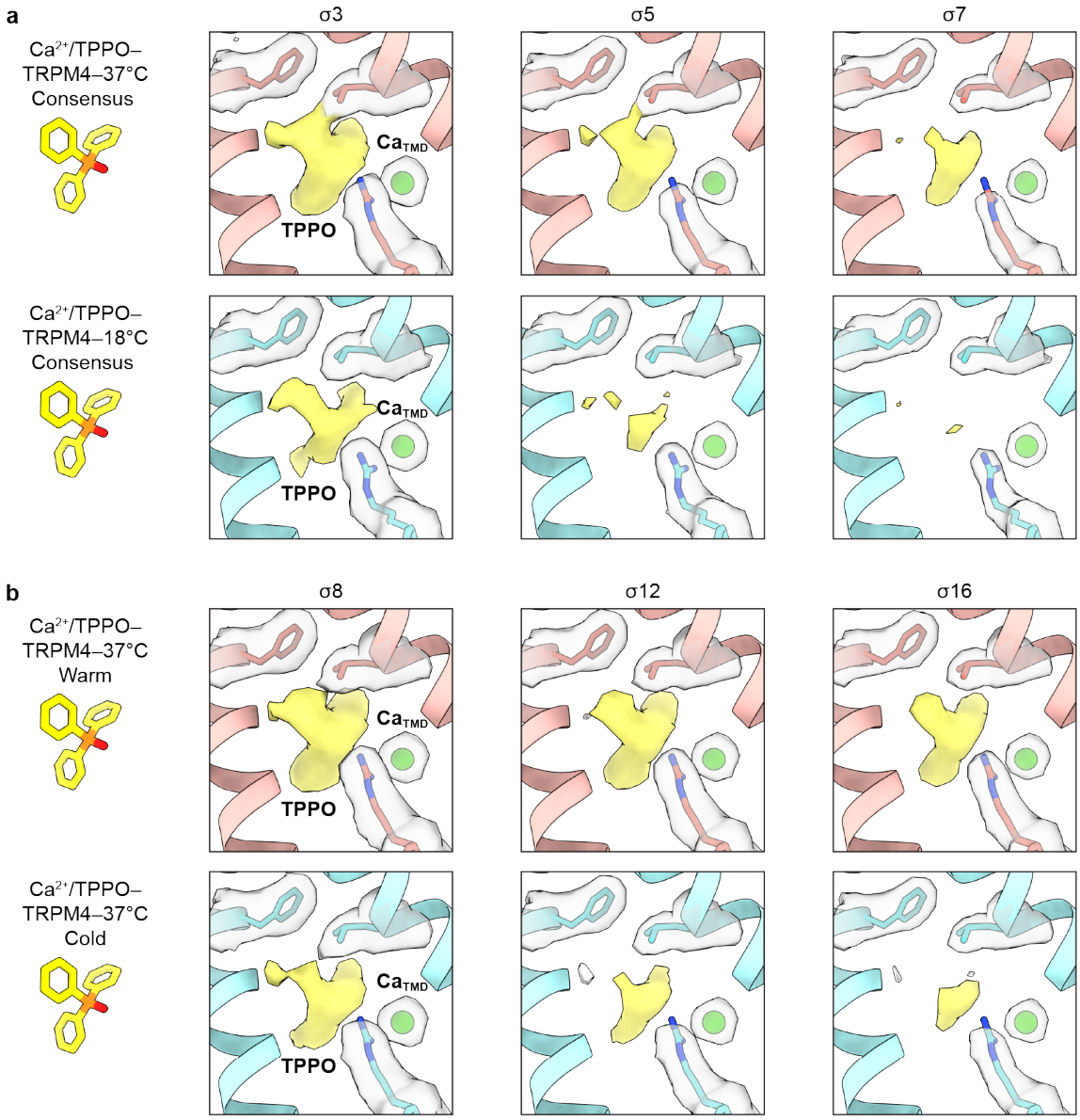

Extended Data Figure 7. Densities of the TPPO binding site from various datasets or conformations contoured at different σ levels.

Densities at the TPPO binding site are shown as yellow surfaces. For comparison, densities for Ca_{TMD} and surrounding interacting residues are displayed as transparent surfaces. The TPPO molecule in the pose fitted to the Ca^{2+}/TPPO–TRPM4–37 °C warm map is shown on the left in stick representation.

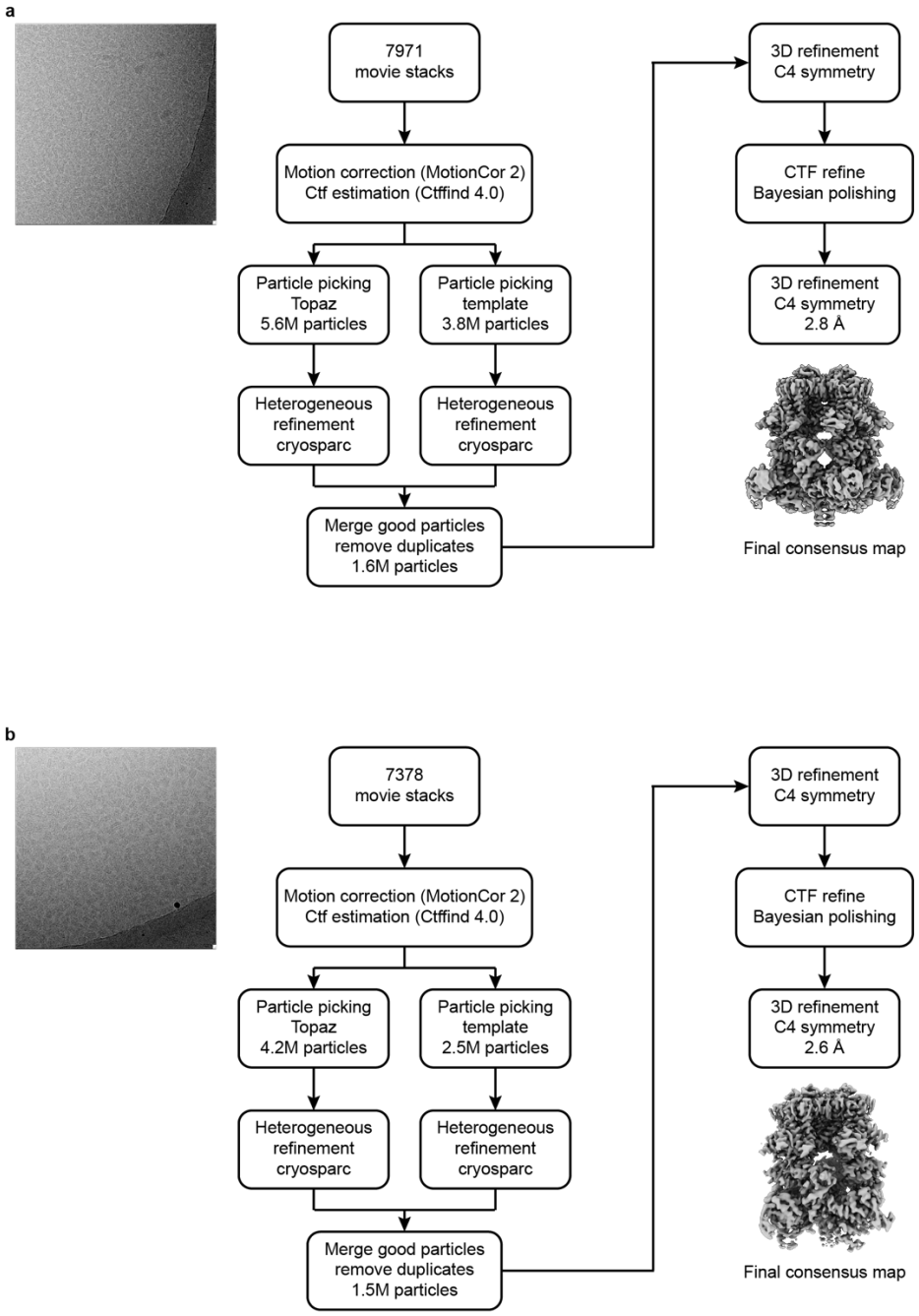

Extended Data Figure 8. Cryo-EM data processing workflow for the Ca^{2+}/NC1–TRPM4–37 °C (a) and EGTA/NC1–TRPM4–18 °C (b) datasets. Representative micrographs are shown. The final maps are displayed with their respective resolutions.

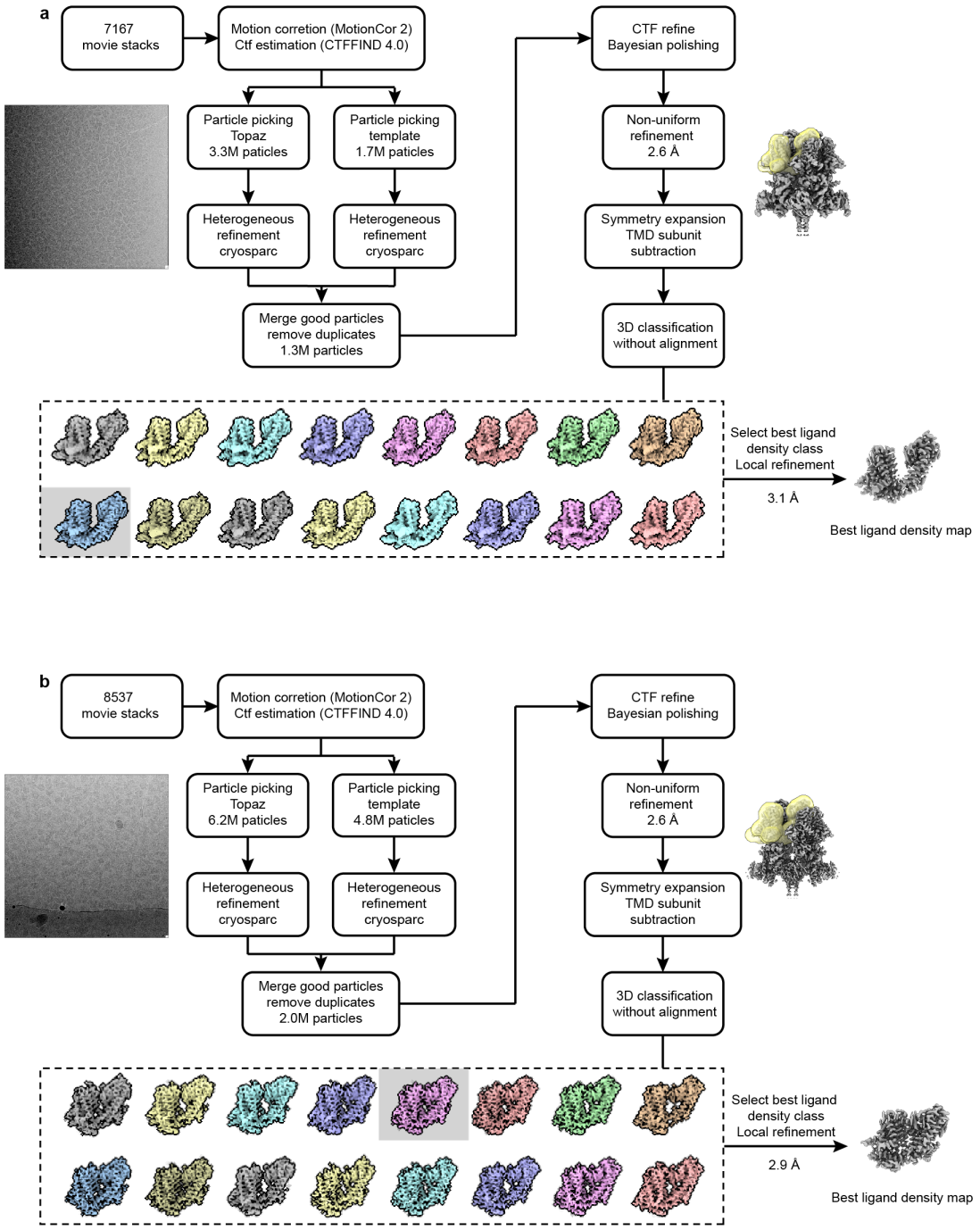

Extended Data Figure 9. Cryo-EM data processing workflow for the Ca^{2+}/CBA–TRPM4–18 °C (a) and Ca^{2+}/CBA–TRPM4–37 °C (b) datasets. Representative micrographs are shown. The final consensus map and the TMD-focused map with the best-resolved ligand density are displayed with their respective resolutions.

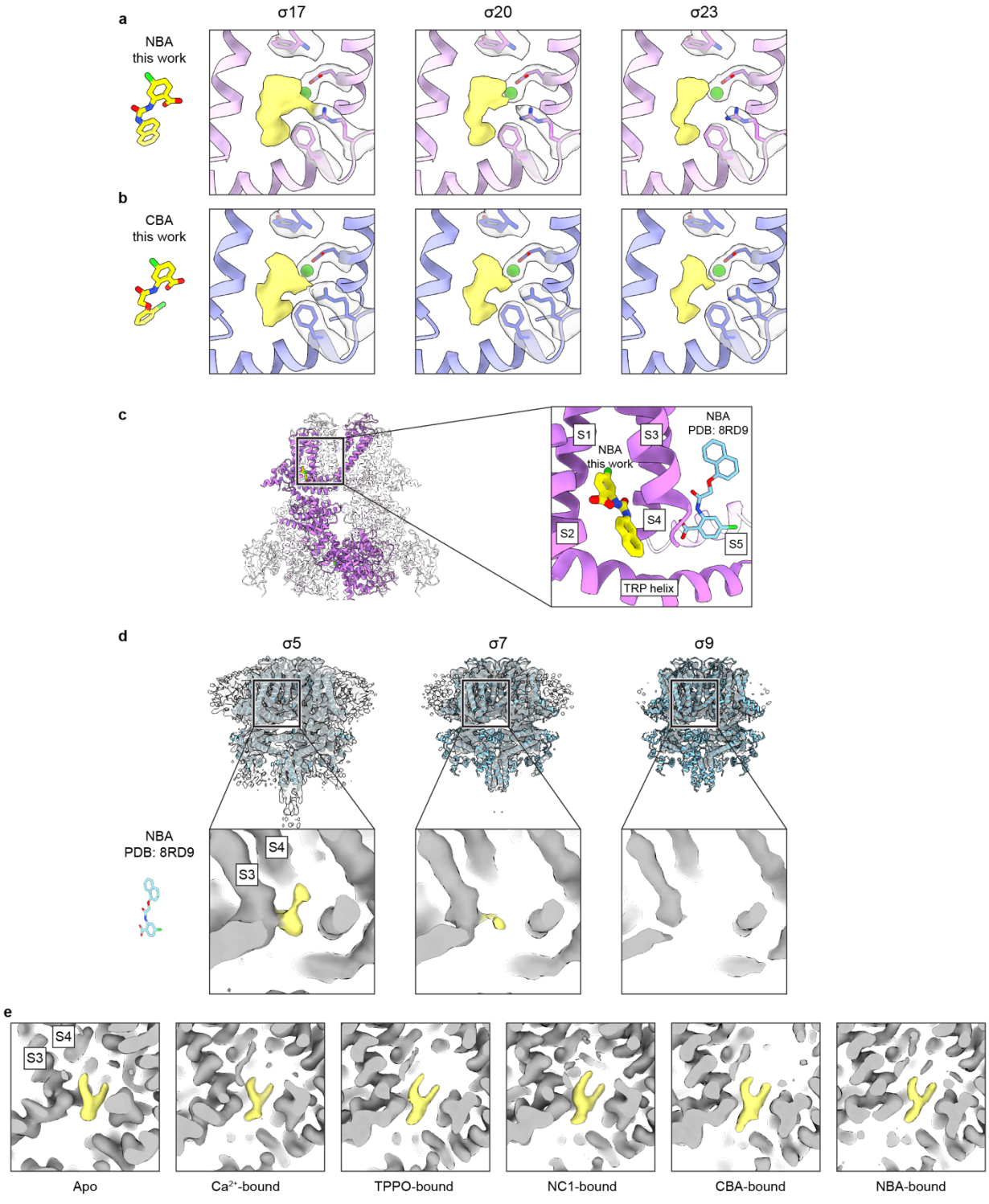

Extended Data Figure 10. Comparison of the NBA and CBA sites identified in this study with the previously reported NBA site, along with the densities observed within these sites.

669 **a**,**b**, NBA and CBA densities contoured at different σ levels for the Ca^{2+}/NBA–TRPM4–37 °C
670 TMD map and the Ca^{2+}/CBA–TRPM4–37 °C TMD map in this study. Densities of NBA and
671 CBA are shown as yellow surfaces. For comparison, densities for Ca_{TMD} and surrounding
672 interacting residues are displayed as transparent surfaces. The NBA and CBA molecules in the
673 poses fitted to the maps are shown on the left in stick representation. **c**, Location of the NBA
674 binding site identified in this work (yellow; PDB-ID 9Z24) compared with the previously
675 reported site (light blue; PDB-ID 8RD9). **d**, The overall cryo-EM map (top) and the densities of
676 the putative NBA binding site (bottom) from the previously published TRPM4 structure in the
677 presence of NBA (EMD-19069), contoured at different σ levels. The putative NBA densities are
678 highlighted in yellow, and the protein densities are shown in gray. The NBA molecule in the pose
679 fitted to the map is shown on the left in stick representation. **e**, Densities at the previously
680 reported NBA binding site in our high-resolution cryo-EM maps across different ligand
681 conditions consistently reveal a Y-shaped density characteristic of a lipid molecule. The Y-shaped
682 densities are highlighted in yellow, and the protein densities are shown in gray.

683

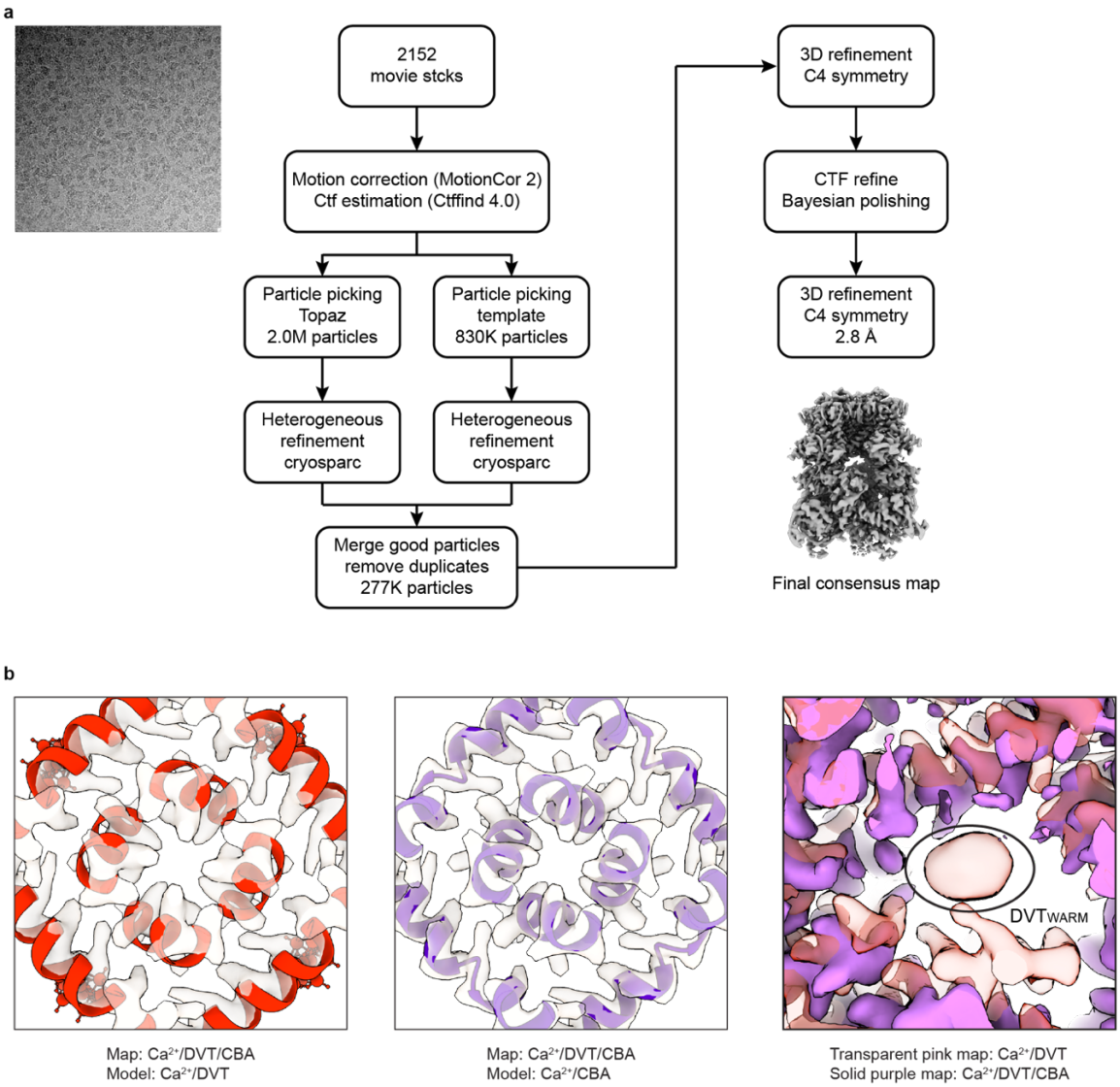

Extended Data Figure 11. Cryo-EM data processing workflow for the Ca^{2+}/DVT/CBA–TRPM4–18 °C dataset. a, A representative micrograph is shown. The final map is displayed with the resolution. **b**, Left: superimposition of the Ca^{2+}/DVT/CBA–TRPM4 map and the Ca^{2+}/DVT–TRPM4$_{Warm}$ model (red; open state), focusing on the transmembrane domain, viewed from the intracellular side. Middle: Superimposition of the Ca^{2+}/DVT/CBA–TRPM4 map and the Ca^{2+}/CBA–TRPM4 model (purple), focusing on the transmembrane domain, viewed from the intracellular side. Right: superimposition of the cryo-EM maps of Ca^{2+}/DVT/–TRPM4$_{Warm}$ (transparent pink) and Ca^{2+}/DVT/CBA–TRPM4 (solid purple), focusing on the DVT$_{Warm}$ site and its surroundings.

	Ca^{2+}/TPPO–TRPM4–37°C (EMDB-73754) (PDB 9Z1W)	Ca^{2+}/TPPO–TRPM4–37°C warm TMD (EMDB-73755) (PDB 9Z1X)	Ca^{2+}/TPPO–TRPM4–37°C cold TMD (EMDB-73756) (PDB 9Z1Y)	Ca^{2+}/TPPO–TRPM4–18°C (EMDB-73757) (PDB 9Z1Z)	EGTA/TPPO–TRPM4–37°C (EMDB-73758) (PDB 9Z20)
Data collection and processing					
Magnification	135000	135000	135000	135000	135000
Voltage (kV)	200	200	200	200	200
Electron exposure (e–/Å^2)	40	40	40	40	40
Defocus range (μm)	-0.5 – -1.4	-0.5 – -1.4	-0.5 – -1.4	-0.5 – -1.4	-0.5 – -1.4
Pixel size (Å)	0.87	0.87	0.87	0.87	0.874
Symmetry imposed	C4	C1	C1	C1	C4
Initial particle images (no.)	2.6M			2.7M	4.9M
Final particle images (no.)	1180K	882K	294K	760K	1929K
Map resolution (Å)	2.9	3.0	3.3	2.6	2.5
FSC threshold	0.143	0.143	0.143	0.143	0.143
Map resolution range (Å)	2.9 – 246.2	3.0 – 246.2	3.2 – 246.2	2.6 – 246.2	2.5 – 246.2
Refinement					
Initial model used (PDB code)	5WP6	5WP6	5WP6	5WP6	5WP6
Model resolution (Å)	3.3	3.3	3.5	3.1	2.7
FSC threshold	0.5	0.5	0.5	0.5	0.5
Model resolution range (Å)	3.3 – 246.2	3.3 – 246.2	3.5 – 246.2	3.1 – 246.2	2.7 – 246.2
Map sharpening *B* factor (Å^2)	-120	-30	-30	-100	-100
Model composition					
Non-hydrogen atoms	30220	2912	2912	29272	29312
Protein residues	3976	365	365	3892	3896
Ligands	12	2	2	12	0
B factors (Å^2)					
Protein	133.28	83.39	82.41	123.92	103.06
Ligand	144.31	98.78	95.88	78.23	
R.m.s. deviations					
Bond lengths (Å)	0.004	0.003	0.002	0.006	0.003
Bond angles (°)	0.469	0.448	0.419	0.493	0.452
Validation					
MolProbity score	1.21	1.13	1.10	1.14	0.92
Clashscore	1.89	2.41	2.24	1.69	0.97
Poor rotamers (%)	0.68	0	0	0.5	1.13
Ramachandran plot					
Favored (%)	96.15	97.49	97.49	96.63	97.58
Allowed (%)	3.85	2.51	2.51	3.37	2.42
Disallowed (%)	0	0	0	0	0

Extended Data Table 1: Cryo-EM data collection, refinement and validation statistics. Data are shown for Ca^{2+}/TPPO–TRPM4–37°C, Ca^{2+}/TPPO–TRPM4–37°C warm TMD, Ca^{2+}/TPPO–TRPM4–37°C cold TMD, Ca^{2+}/TPPO–TRPM4–18°C, and EGTA/TPPO–TRPM4–37°C.

	Ca^{2+}/NC1–TRPM4–37°C (EMDB-73759) (PDB 9Z21)	EGTA/NC1–TRPM4–37°C (EMDB-73760) (PDB 9Z22)	Ca^{2+}/CBA–TRPM4–37°C (EMDB-73761) (PDB 9Z23)	Ca^{2+}/CBA–TRPM4–37°C TMD (EMDB-73762) (PDB 9Z24)	Ca^{2+}/NBA–TRPM4–37°C (EMDB-73763) (PDB 9Z25)
Data collection and processing					
Magnification	135000	135000	135000	135000	135000
Voltage (kV)	200	200	200	200	200
Electron exposure (e–/Å^2)	40	40	40	40	40
Defocus range (μm)	-0.5 – -1.4	-0.5 – -1.4	-0.5 – -1.4	-0.5 – -1.4	-0.5 – -1.4
Pixel size (Å)	0.874	0.87	0.87	0.87	0.874
Symmetry imposed	C4	C4	C4	C1	C4
Initial particle images (no.)	5.6M	4.2M	3.3M		6.2M
Final particle images (no.)	1636K	1475K	1290K	160K	2049K
Map resolution (Å)	2.8	2.6	2.6	3.1	2.6
FSC threshold	0.143	0.143	0.143	0.143	0.143
Map resolution range (Å)	2.8 – 246.2	2.6 – 246.2	2.6 – 246.2	3.1 – 246.2	2.6 – 246.2
Refinement					
Initial model used (PDB code)	5WP6	5WP6	5WP6	5WP6	5WP6
Model resolution (Å)	3.1	2.9	3.2	3.3	2.9
FSC threshold	0.5	0.5	0.5	0.5	0.5
Model resolution range (Å)	3.1 – 246.2	2.9 – 246.2	3.2 – 246.2	3.3 – 246.2	2.9 – 246.2
Map sharpening *B* factor (Å^2)	-117	-105	-102	-50	-106
Model composition					
Non-hydrogen atoms	30300	29396	30304	2740	30300
Protein residues	3976	3900	3972	338	3972
Ligands	12	4	12	2	12
B factors (Å^2)					
Protein	107.36	100.17	108.2	101.63	114.79
Ligand	117.04	83.25	66.02	116.92	82.15
R.m.s. deviations					
Bond lengths (Å)	0.004	0.004	0.004	0.004	0.003
Bond angles (°)	0.488	0.439	0.460	0.468	0.440
Validation					
MolProbity score	1.36	1.44	1.22	1.2	1.34
Clashscore	2.14	4.57	1.6	2.19	2.35
Poor rotamers (%)	0.27	0.14	1.08	0.35	0.27
Ramachandran plot					
Favored (%)	94.62	96.74	95.79	96.69	95.28
Allowed (%)	5.38	3.26	4.21	3.31	4.72
Disallowed (%)	0	0	0	0	0

Extended Data Table 1: Cryo-EM data collection, refinement and validation statistics. Data are shown for Ca^{2+}/NC1–TRPM4–37°C, EGTA/NC1–TRPM4–37°C, Ca^{2+}/CBA–TRPM4–37°C, and Ca^{2+}/NBA–TRPM4–37°C.

	Ca^{2+}/NBA–TRPM4–37°C TMD (EMDB-73764) (PDB 9Z26)	Ca^{2+}/CBA/DVT–TRPM4–37°C (EMDB-73765) (PDB 9Z27)
Data collection and processing		
Magnification	135000	135000
Voltage (kV)	200	200
Electron exposure (e–/Å^2)	40	40
Defocus range (μm)	-0.5 – -1.4	-0.5 – -1.4
Pixel size (Å)	0.874	0.87
Symmetry imposed	C1	C4
Initial particle images (no.)		2M
Final particle images (no.)	239K	278K
Map resolution (Å)	2.9	2.8
FSC threshold	0.143	0.143
Map resolution range (Å)	2.9 – 246.2	3.8 – 246.2
Refinement		
Initial model used (PDB code)	5WP6	5WP6
Model resolution (Å)	3.2	3.2
FSC threshold	0.5	0.5
Model resolution range (Å)	3.2 – 246.2	3.2 – 246.2
Map sharpening *B* factor (Å^2)	-50	-95
Model composition		
Non-hydrogen atoms	2945	30292
Protein residues	364	3972
Ligands	2	12
B factors (Å^2)		
Protein	110.32	191.28
Ligand	125.37	118.86
R.m.s. deviations		
Bond lengths (Å)	0.004	0.002
Bond angles (°)	0.499	0.466
Validation		
MolProbity score	1.11	1.34
Clashscore	2.72	3.37
Poor rotamers (%)	0.97	0.54
Ramachandran plot		
Favored (%)	97.77	96.64
Allowed (%)	2.23	3.36
Disallowed (%)	0	0

703

704 **Extended Data Table 1: Cryo-EM data collection, refinement and validation statistics.** Data
705 are shown for Ca^{2+}/NBA–TRPM4–37°C TMD, and Ca^{2+}/DVT/CBA–TRPM4–37°C.

706 **Data Availability**

707 Cryo-EM density maps have been deposited at the EMDB (Electron Microscopy Data Bank) and
708 the Research Collaboratory for Structural Bioinformatics Protein Data Bank (RCS-PDB),
709 respectively.

710 **Acknowledgements**

711 We thank for the support with data collection at the Structural Biology Facility at Northwestern
712 University. We appreciate the Structural Biology Facility and Northwestern IT Research
713 Computing and Data Services for computational support. W.L. is supported by National
714 Institutes of Health (NIH) grants (R01HL153219 and R01NS112363, and R35GM138321). J.D.
715 is supported by a McKnight Scholar Award, a Klingenstein-Simon Scholar Award, a Sloan
716 Research Fellowship in neuroscience, a Pew Scholar in the Biomedical Sciences award, and NIH
717 grants (R01NS111031 and R01NS129804). J.H. is supported by American Heart Association
718 postdoctoral fellowship (24POST1196982).

719 **Author Contributions**

720 J.D. and W.L. supervised the project. J.H. carried out mutagenesis, protein purification, cryo-EM
721 data collection and processing, and structural analysis for all TRPM4 structures included in the
722 study. S.I. and J.C. contributed to the initial cryo-EM studies of TRPM4 in complex with NBA,
723 CBA, and NC1. S.P. and J.L. performed functional experiments. G.O. and J.S. carried out
724 mutagenesis and expression test. J.H., J.D. and W.L. wrote the manuscript, with contributions
725 from S.P. and J.L. All authors participated in manuscript preparation and approved the final
726 version. The authors declare no conflicts of interest.

727

728 **Methods**

729 **Human TRPM4 protein expression and purification**

730 The gene encoding human full-length TRPM4 (UniProtKB: Q8TD43) was subcloned into pEG
731 BacMam vector with a 2×Strep tag, GFP and a thrombin-cleavage site at the N terminus[53].
732 Bacmid and baculovirus of TRPM4 in a BacMam vector were generated, and P2 viruses were
733 used to infect a suspension of tsA cells. Cells were incubated at 37 °C for 8 h and10 mM sodium
734 butyrate was added to the culture and the temperature was changed to 30 °C. The cells were
735 collected 72 h after infection and resuspended in a buffer containing 100 mM Tris pH 8.0 and
736 150 mM NaCl (TBS buffer) in the presence of 1 mM phenylmethylsulphonyl fluoride, 0.8 μM
737 aprotinin, 2 μg ml^{-1} leupeptin and 2 mM pepstatin A. The cells were lysed by sonication and the
738 membrane fraction was collected by centrifugation at 186,000*g* using a 45 Ti rotor (Beckman
739 Coulter) for 1 h at 4 °C. The membrane then homogenized with a Dounce homogenizer in TBS
740 buffer supplemented with protease inhibitors. The protein was extracted from the membrane with
741 TBS buffer supplemented with 1% GDN and protease inhibitors for 3 h at 4 °C. The solubilized
742 proteins were loaded to Strep-Tactin resin. After washing with TBS buffer supplemented with
743 0.02% GDN, TRPM4 was eluted with the same buffer, supplemented with 10 mM desthiobiotin.
744 The GFP tag were cleaved, and proteins were concentrated and further purified by size-exclusion
745 chromatography (Superose 6). The peak fractions containing the TRPM4 were pooled and
746 concentrated to 8 mg ml^{-1}.

747 **EM sample preparation and data acquisition**

748 Purified TRPM4 was incubated with 5 mM calcium chloride or 5 mM EGTA, as required for
749 each experiment, for 30 s at 18 or 37 °C. Then 0.1mM TPPO, 0.25mM CBA/NBA or 0.8mM
750 NC1 was added and further incubation for 2 min at 18 or 37 °C respectively. 2.5 μl sample was
751 applied to a glow-discharged Quantifoil holey carbon grid (gold, 2/1 μm size/hole space, 300
752 mesh). The grids were blotted for 1.5 s in the Vitrobot Mark III set to 100% humidity and 37 °C
753 with a 15 s wait time before being plunge-frozen into liquid ethane cooled by liquid nitrogen.

754 For the all the sample, images were recorded using the FEI Glacios electron microscope at
755 200 kV and a nominal magnification of 135,000×. A Falcon 4i direct electron detector with

Selectris energy filter was used resulting a pixel size of 0.87 Å or 0.874 Å. EPU was used for automated acquisition. Nominal defocus ranged from −0.5 to −1.4 μm.

Cryo-electron microscopy data analysis procedure

The detailed workflow for the data-processing procedure is summarized in Extended Data Figs. 4–5, 8, 9, 11. In general, the raw movies for each dataset were motion-corrected using MotionCor2 (v.1.1.0)[54]. The per-micrograph defocus values were estimated using ctffind (v.4.1.10)[55]. Particle picking was performed using relion template picker[56] and topaz (v.0.2.4)[57]. Junk particles were removed by rounds of 3D heterogeneous refinement using CryoSPARC[58]. Good particles were selected for non-uniformed refinement with C_4 symmetry in CryoSPARC to generate a 3D map. Multiple rounds of CTF refinement and Bayesian polishing were performed in RELION and CryoSPARC to further improve the map resolution.

For 37 °C with Ca^{2+} and TPPO dataset, symmetry expansion at the single subunit of ICD level was done from the map refined with C_4 symmetry, followed by monomer ICD subtraction. The subtracted images of the monomer ICD underwent 3D classification without image alignment in RELION to identify the warm and cold conformation. The correspond warm and cold monomer were subsequently undergone similar TMD monomer 3D classification to identify the best the local resolution map with the bound ligand.

For the rest of 37 °C with Ca^{2+} dataset, symmetry expansion at the single subunit of TMD level was done from the map refined with C_4 symmetry, followed by monomer TMD subtraction. The subtracted images of the monomer TMD underwent 3D classification without image alignment in RELION to identify the class with the best local resolution map with the bound ligand.

Map resolution estimates were based on the gold standard Fourier shell correlation 0.143 criterion for all datasets.

Model building

Atomic models were generated by rigid-body fitting of the TMD, MHR1/2 and MHR3/4 and C-terminal domains from a published human TRPM4 model (PDB: 5WP6) into the final cryo-EM maps. Ligands were fitted into the density through real-space refinement using COOT[59]. The CIF file of ligands was generated using grade web server (Global Phasing Ltd.). The models were

then manually adjusted in COOT and subjected to phenix.real_space_refine[60] to improve the model metrics. The final models were validated using phenix.molprobity[61]. Figures were generated using UCSF ChimeraX[62].

Electrophysiology

TsA201 cells expressing plasmids encoding N-terminal GFP-tagged human TRPM4 WT and mutants were used. One day after transfection with plasmid DNA (100 ng ml^{-1}) and Lipofectamine 2000 (Invitrogen, 11668019), the cells were trypsinized and replated onto poly-L-lysine-coated (Sigma, P4707) glass coverslips. After cell attachment, the coverslip was transferred to a recording chamber. Whole-cell patch-clamp recordings were performed at room temperature (21–23 °C) or body temperature (36–38 °C). The temperature of perfusion solutions was controlled by thermal control devices (SC-20/CL-100, Warner Instruments).

For whole-cell recordings, glass pipettes were pulled to 3–5 MΩ and filled with an internal solution. Signals were amplified with a MultiClamp 700B amplifier (controlled by MultiClamp Commander v2.2.2.2) and digitized using a Digidata 1550B A/D converter controlled by Clampex v11.3 (Molecular Devices). Whole-cell currents were measured in cells with an access resistance of < 10 MΩ after achieving whole-cell configuration. Whole-cell capacitance was compensated by the amplifier circuitry. Whole-cell currents were recorded using a two-step voltage protocol in which cells were held at –100 mV for 200 ms and then stepped to +100 mV for another 200 ms, repeated every 10 s. An alternative voltage-step protocol was applied, in which cells were stepped from –100 mV to +140 mV in 20-mV increments, with each step lasting 100 ms. A voltage ramp from –100 to +100 mV (200 ms duration) was applied every 5 s from a holding potential of 0 mV. Data were sampled at 10 kHz and low-pass filtered at 2 kHz. Recordings were analyzed using Clampfit v11.3 (Axon Instruments), GraphPad Prism v10.6.1 (GraphPad Software, Inc., La Jolla, CA), and OriginPro 2024 (OriginLab, Northampton, MA). Data were also analyzed using custom Python scripts, including pyABF for loading and processing ABF electrophysiology files. Electrophysiology files were parsed and analyzed in Python v3.11.8 executed in Spyder v6.0.7 (Anaconda environment) on macOS v26.0.1 (ARM architecture). Data processing used pandas v2.2.2 and numerical operations used NumPy v1.26.4. All custom analysis scripts used in this study are available at https://github.com/junuk861/ephys-analysis-scripts. The bath solution (pH 7.4) contained 150

814 mM NaCl, 3 mM KCl, 10 mM HEPES, 2 mM $CaCl_2$, 1 mM $MgCl_2$, and 12 mM mannitol. Patch
815 pipettes were filled with internal solutions containing 150 mM NaCl, 1 mM $MgCl_2$, 10 mM
816 HEPES, 5 mM EGTA, and $CaCl_2$ adjusted (0 or 1.69 mM) to yield 0 or 0.1 μM free Ca^{2+},
817 respectively (pH 7.3,
818 22 °C) (source: https://somapp.ucdmc.ucdavis.edu/pharmacology/bers/maxchelator/CaEGTA-
819 TS.htm). For whole-cell recordings of NC1-induced and NBA/CBA-inhibited currents, the
820 extracellular solution contained the following (in mM): 150 NaCl, 10 HEPES and 1 $MgCl_2$. The
821 intracellular solution contained (in mM): 150 NaCl, 10 HEPES and 5 EGTA. The intracellular
822 concentration of $CaCl_2$ was set to either 0, 1.69 or 4.45 mM (corresponding to 0, 0.1 or 1 μM of
823 free Ca^{2+}). The pH was adjusted to 7.4 using NaOH in both the extracellular and intracellular
824 solutions.

825 TPPO (Sigma-Aldrich, T84603) was prepared daily as a 70 mM stock solution in ethanol and
826 diluted to the desired final concentration in the bath solution immediately before use. NC1
827 (Necrocide 1, MCE, HY-14307), NBA (4-chloro-2-(2-(naphthalen-1-yloxy)acetamido)benzoic
828 acid, MCE, HY-128172), and CBA (4-chloro-2-[2-(2-chloro-phenoxy)-acetylamino]-benzoic
829 acid, Tocris, 6724) were dissolved in DMSO to a stock concentration of 10, 100, and 50 mM,
830 respectively.

831

832

833 **References**

834 1 Gao, Y., Cao, E., Julius, D. & Cheng, Y. TRPV1 structures in nanodiscs reveal
835 mechanisms of ligand and lipid action. *Nature* **534**, 347-351 (2016).
836 https://doi.org/10.1038/nature17964
837 2 Yang, X. *et al*. Structure deformation and curvature sensing of PIEZO1 in lipid
838 membranes. *Nature* **604**, 377-383 (2022). https://doi.org/10.1038/s41586-022-
839 04574-8
840 3 Yao, X., Fan, X. & Yan, N. Cryo-EM analysis of a membrane protein embedded in the
841 liposome. *Proc Natl Acad Sci U S A* **117**, 18497-18503 (2020).
842 https://doi.org/10.1073/pnas.2009385117
843 4 Tao, X., Zhao, C. & MacKinnon, R. Membrane protein isolation and structure
844 determination in cell-derived membrane vesicles. *Proc Natl Acad Sci U S A* **120**,
845 e2302325120 (2023). https://doi.org/10.1073/pnas.2302325120

5 Zhou, J. *et al.* Resolving native GABA(A) receptor structures from the human brain. *Nature* **638**, 562-568 (2025). https://doi.org/10.1038/s41586-024-08454-1

6 Lin, S., Ke, M., Zhang, Y., Yan, Z. & Wu, J. Structure of a mammalian sperm cation channel complex. *Nature* **595**, 746-750 (2021). https://doi.org/10.1038/s41586-021-03742-6

7 Zhang, M. *et al.* Assembly and architecture of endogenous NMDA receptors in adult cerebral cortex and hippocampus. *Cell* **188**, 1198-1207 e1113 (2025). https://doi.org/10.1016/j.cell.2025.01.004

8 Jeong, H. *et al.* Structures of the TMC-1 complex illuminate mechanosensory transduction. *Nature* **610**, 796-803 (2022). https://doi.org/10.1038/s41586-022-05314-8

9 Kumar Mondal, A., Carrillo, E., Jayaraman, V. & Twomey, E. C. Glutamate gating of AMPA-subtype iGluRs at physiological temperatures. *Nature* (2025). https://doi.org/10.1038/s41586-025-08770-0

10 Hu, J. *et al.* Physiological temperature drives TRPM4 ligand recognition and gating. *Nature* **630**, 509-515 (2024). https://doi.org/10.1038/s41586-024-07436-7

11 Bootman, M. D. & Bultynck, G. Fundamentals of Cellular Calcium Signaling: A Primer. *Cold Spring Harb Perspect Biol* **12** (2020). https://doi.org/10.1101/cshperspect.a038802

12 Zhang, W. H. *et al.* Association of concomitant H1 antihistamine and immune checkpoint inhibitor therapy on survival outcome and safety in patients with advanced primary lung cancer: a cohort study. *Transl Lung Cancer Res* **13**, 2787-2801 (2024). https://doi.org/10.21037/tlcr-24-795

13 Launay, P. *et al.* TRPM4 is a Ca2+-activated nonselective cation channel mediating cell membrane depolarization. *Cell* **109**, 397-407 (2002). https://doi.org/10.1016/s0092-8674(02)00719-5

14 Nilius, B. *et al.* Voltage dependence of the Ca2+-activated cation channel TRPM4. *J Biol Chem* **278**, 30813-30820 (2003). https://doi.org/10.1074/jbc.M305127200

15 Talavera, K. *et al.* Heat activation of TRPM5 underlies thermal sensitivity of sweet taste. *Nature* **438**, 1022-1025 (2005). https://doi.org/10.1038/nature04248

16 Cheng, H. *et al.* TRPM4 controls insulin secretion in pancreatic beta-cells. *Cell Calcium* **41**, 51-61 (2007). https://doi.org/10.1016/j.ceca.2006.04.032

17 Pironet, A., Vandewiele, F. & Vennekens, R. Exploring the role of TRPM4 in calcium-dependent triggered activity and cardiac arrhythmias. *J Physiol* **602**, 1605-1621 (2024). https://doi.org/10.1113/JP283831

18 Vandewiele, F. *et al.* TRPM4 inhibition by meclofenamate suppresses Ca2+-dependent triggered arrhythmias. *Eur Heart J* **43**, 4195-4207 (2022). https://doi.org/10.1093/eurheartj/ehac354

19 Yan, J., Bengtson, C. P., Buchthal, B., Hagenston, A. M. & Bading, H. Coupling of NMDA receptors and TRPM4 guides discovery of unconventional neuroprotectants. *Science* **370** (2020). https://doi.org/10.1126/science.aay3302

20 Menigoz, A. *et al.* TRPM4-dependent post-synaptic depolarization is essential for the induction of NMDA receptor-dependent LTP in CA1 hippocampal neurons. *Pflugers Arch* **468**, 593-607 (2016). https://doi.org/10.1007/s00424-015-1764-7

21 Schattling, B. *et al.* TRPM4 cation channel mediates axonal and neuronal degeneration in experimental autoimmune encephalomyelitis and multiple sclerosis. *Nat Med* **18**, 1805-1811 (2012). https://doi.org/10.1038/nm.3015
22 Shimizu, T. *et al.* TRPM4 regulates migration of mast cells in mice. *Cell Calcium* **45**, 226-232 (2009). https://doi.org/10.1016/j.ceca.2008.10.005
23 Barbet, G. *et al.* The calcium-activated nonselective cation channel TRPM4 is essential for the migration but not the maturation of dendritic cells. *Nat Immunol* **9**, 1148-1156 (2008). https://doi.org/10.1038/ni.1648
24 Guinamard, R., Demion, M., Chatelier, A. & Bois, P. Calcium-activated nonselective cation channels in mammalian cardiomyocytes. *Trends Cardiovasc Med* **16**, 245-250 (2006). https://doi.org/10.1016/j.tcm.2006.04.007
25 Liu, Y. *et al.* Noncanonical calcium-independent TRPM4 activation governs intestinal fluid homeostasis. *Nat Commun* (2026). https://doi.org/10.1038/s41467-025-68014-7
26 Dai, Y., Wang, H., Wang, W. & Zhuang, X. Multidimensional pan cancer analysis of the sodium induced cell death gene TRPM4. *Sci Rep* **15**, 29768 (2025). https://doi.org/10.1038/s41598-025-15082-w
27 Guo, J. *et al.* TRPM4 channels contribute to Adriamycin chemoresistance in breast cancer cells. *Eur J Pharmacol* **998**, 177637 (2025). https://doi.org/10.1016/j.ejphar.2025.177637
28 Kappel, S. *et al.* TRPM4 is highly expressed in human colorectal tumor buds and contributes to proliferation, cell cycle, and invasion of colorectal cancer cells. *Mol Oncol* **13**, 2393-2405 (2019). https://doi.org/10.1002/1878-0261.12566
29 Sagredo, A. I. *et al.* TRPM4 regulates Akt/GSK3-beta activity and enhances beta-catenin signaling and cell proliferation in prostate cancer cells. *Mol Oncol* **12**, 151-165 (2018). https://doi.org/10.1002/1878-0261.12100
30 Gualandi, F. *et al.* Mutation Load of Multiple Ion Channel Gene Mutations in Brugada Syndrome. *Cardiology* **137**, 256-260 (2017). https://doi.org/10.1159/000471792
31 Saito, Y. *et al.* TRPM4 Mutation in Patients With Ventricular Noncompaction and Cardiac Conduction Disease. *Circ Genom Precis Med* **11**, e002103 (2018). https://doi.org/10.1161/CIRCGEN.118.002103
32 Hof, T. *et al.* TRPM4 non-selective cation channel variants in long QT syndrome. *BMC Med Genet* **18**, 31 (2017). https://doi.org/10.1186/s12881-017-0397-4
33 Liu, H. *et al.* Molecular genetics and functional anomalies in a series of 248 Brugada cases with 11 mutations in the TRPM4 channel. *PLoS One* **8**, e54131 (2013). https://doi.org/10.1371/journal.pone.0054131
34 Liu, H. *et al.* Gain-of-function mutations in TRPM4 cause autosomal dominant isolated cardiac conduction disease. *Circ Cardiovasc Genet* **3**, 374-385 (2010). https://doi.org/10.1161/CIRCGENETICS.109.930867
35 Palmer, R. K. *et al.* Triphenylphosphine oxide is a potent and selective inhibitor of the transient receptor potential melastatin-5 ion channel. *Assay Drug Dev Technol* **8**, 703-713 (2010). https://doi.org/10.1089/adt.2010.0334

932 36 Fu, W. *et al.* Persistent activation of TRPM4 triggers necrotic cell death characterized
933 by sodium overload. *Nat Chem Biol* **21**, 1238-1249 (2025).
934 https://doi.org/10.1038/s41589-025-01841-3
935 37 Ozhathil, L. C. *et al.* Identification of potent and selective small molecule inhibitors
936 of the cation channel TRPM4. *Br J Pharmacol* **175**, 2504-2519 (2018).
937 https://doi.org/10.1111/bph.14220
938 38 Bochen, F. *et al.* TRPM4 contributes to cell death in prostate cancer tumor
939 spheroids, and to extravasation and metastasis in a zebrafish xenograft model
940 system. *Mol Oncol* **19**, 1299-1309 (2025). https://doi.org/10.1002/1878-0261.13795
941 39 Nilius, B., Prenen, J., Voets, T. & Droogmans, G. Intracellular nucleotides and
942 polyamines inhibit the Ca2+-activated cation channel TRPM4b. *Pflugers Arch* **448**,
943 70-75 (2004). https://doi.org/10.1007/s00424-003-1221-x
944 40 Ekundayo, B. *et al.* Identification of a binding site for small molecule inhibitors
945 targeting human TRPM4. *Nat Commun* **16**, 833 (2025).
946 https://doi.org/10.1038/s41467-025-56131-2
947 41 Cao, E., Liao, M., Cheng, Y. & Julius, D. TRPV1 structures in distinct conformations
948 reveal activation mechanisms. *Nature* **504**, 113-118 (2013).
949 https://doi.org/10.1038/nature12823
950 42 Ruan, Z. *et al.* Structures of the TRPM5 channel elucidate mechanisms of activation
951 and inhibition. *Nat Struct Mol Biol* **28**, 604-613 (2021).
952 https://doi.org/10.1038/s41594-021-00607-4
953 43 Guo, J. *et al.* Structures of the calcium-activated, non-selective cation channel
954 TRPM4. *Nature* **552**, 205-209 (2017). https://doi.org/10.1038/nature24997
955 44 Autzen, H. E. *et al.* Structure of the human TRPM4 ion channel in a lipid nanodisc.
956 *Science* **359**, 228-232 (2018). https://doi.org/10.1126/science.aar4510
957 45 Winkler, P. A., Huang, Y., Sun, W., Du, J. & Lu, W. Electron cryo-microscopy structure
958 of a human TRPM4 channel. *Nature* **552**, 200-204 (2017).
959 https://doi.org/10.1038/nature24674
960 46 Huang, Y., Kumar, S., Lee, J., Lu, W. & Du, J. Coupling enzymatic activity and gating in
961 an ancient TRPM chanzyme and its molecular evolution. *Nat Struct Mol Biol* **31**,
962 1509-1521 (2024). https://doi.org/10.1038/s41594-024-01316-4
963 47 Nilius, B., Prenen, J., Janssens, A., Voets, T. & Droogmans, G. Decavanadate
964 modulates gating of TRPM4 cation channels. *J Physiol* **560**, 753-765 (2004).
965 https://doi.org/10.1113/jphysiol.2004.070839
966 48 Yin, Y. *et al.* Molecular basis of neurosteroid and anticonvulsant regulation of
967 TRPM3. *Nat Struct Mol Biol* **32**, 828-840 (2025). https://doi.org/10.1038/s41594-024-
968 01463-8
969 49 Kumar, S. *et al.* Structural basis for agonist and heat activation of nociceptor TRPM3.
970 *Nat Struct Mol Biol* (2025). https://doi.org/10.1038/s41594-025-01692-5
971 50 Diver, M. M., Cheng, Y. & Julius, D. Structural insights into TRPM8 inhibition and
972 desensitization. *Science* **365**, 1434-1440 (2019).
973 https://doi.org/10.1126/science.aax6672
974 51 Yin, Y. *et al.* Structural basis of cooling agent and lipid sensing by the cold-activated
975 TRPM8 channel. *Science* **363** (2019). https://doi.org/10.1126/science.aav9334

52 Zhao, C. *et al.* Structures of a mammalian TRPM8 in closed state. *Nat Commun* **13**, 3113 (2022). https://doi.org/10.1038/s41467-022-30919-y

53 Goehring, A. *et al.* Screening and large-scale expression of membrane proteins in mammalian cells for structural studies. *Nat Protoc* **9**, 2574-2585 (2014). https://doi.org/10.1038/nprot.2014.173

54 Zheng, S. Q. *et al.* MotionCor2: anisotropic correction of beam-induced motion for improved cryo-electron microscopy. *Nat Methods* **14**, 331-332 (2017). https://doi.org/10.1038/nmeth.4193

55 Rohou, A. & Grigorieff, N. CTFFIND4: Fast and accurate defocus estimation from electron micrographs. *J Struct Biol* **192**, 216-221 (2015). https://doi.org/10.1016/j.jsb.2015.08.008

56 Scheres, S. H. RELION: implementation of a Bayesian approach to cryo-EM structure determination. *J Struct Biol* **180**, 519-530 (2012). https://doi.org/10.1016/j.jsb.2012.09.006

57 Bepler, T., Kelley, K., Noble, A. J. & Berger, B. Topaz-Denoise: general deep denoising models for cryoEM and cryoET. *Nat Commun* **11**, 5208 (2020). https://doi.org/10.1038/s41467-020-18952-1

58 Punjani, A., Rubinstein, J. L., Fleet, D. J. & Brubaker, M. A. cryoSPARC: algorithms for rapid unsupervised cryo-EM structure determination. *Nat Methods* **14**, 290-296 (2017). https://doi.org/10.1038/nmeth.4169

59 Emsley, P., Lohkamp, B., Scott, W. G. & Cowtan, K. Features and development of Coot. *Acta Crystallogr D Biol Crystallogr* **66**, 486-501 (2010). https://doi.org/10.1107/S0907444910007493

60 Afonine, P. V. *et al.* Real-space refinement in PHENIX for cryo-EM and crystallography. *Acta Crystallogr D Struct Biol* **74**, 531-544 (2018). https://doi.org/10.1107/S2059798318006551

61 Chen, V. B. *et al.* MolProbity: all-atom structure validation for macromolecular crystallography. *Acta Crystallogr D Biol Crystallogr* **66**, 12-21 (2010). https://doi.org/10.1107/S0907444909042073

62 Pettersen, E. F. *et al.* UCSF Chimera--a visualization system for exploratory research and analysis. *J Comput Chem* **25**, 1605-1612 (2004). https://doi.org/10.1002/jcc.20084